JHEP12 (2015) 051

Resolving boosted jets with XCone

Jesse Thaler and Thomas F. Wilkason

Center for Theoretical Physics, Massachusetts Institute of Technology,
Cambridge, MA, 02139 U.S.A.

E-mail: jthaler@mit.edu, tjwilk@mit.edu

ABSTRACT: We show how the recently proposed XCone jet algorithm [1] smoothly interpolates between resolved and boosted kinematics. When using standard jet algorithms to reconstruct the decays of hadronic resonances like top quarks and Higgs bosons, one typically needs separate analysis strategies to handle the resolved regime of well-separated jets and the boosted regime of fat jets with substructure. XCone, by contrast, is an exclusive cone jet algorithm that always returns a fixed number of jets, so jet regions remain resolved even when (sub)jets are overlapping in the boosted regime. In this paper, we perform three LHC case studies — dijet resonances, Higgs decays to bottom quarks, and all-hadronic top pairs — that demonstrate the physics applications of XCone over a wide kinematic range.

KEYWORDS: Jets, QCD Phenomenology

ARXIV EPRINT: 1508.01518

Contents

1 Introduction

The field of jet substructure has matured significantly over the past five years [2–5], with a variety of techniques in active use at the Large Hadron Collider (LHC) to tag boosted hadronic objects. A prototypical example is the search for heavy new resonances that decay to pairs of top quarks [6, 7]; in the all-hadronic channel, each top quark obtains a large Lorentz boost from the heavy resonance decay, yielding a collimated fat jet with 3-prong substructure. Since not all top quarks are produced in the boosted regime, one should also perform analyses in the resolved regime where the top decay products are well-separated and identified as individual jets. Since new (and old) physics could show up at any energy scale, it is important to develop robust techniques to handle jets in both resolved and boosted kinematics.

In a companion paper, we introduced a new jet algorithm called XCone that blurs the boundary between resolved and boosted kinematics [1]. The name XCone refers to the fact that it is an *exclusive cone* jet algorithm. Like the exclusive k_T algorithm [8], XCone

always returns a fixed number of jets N. When jets are well-separated, XCone yields nearly conical jet regions with radius R. When jets are overlapping, XCone dynamically splits the jet regions into nearest neighbor partitions. Thus, XCone smoothly interpolates between isolated conical jets and merged jets with substructure, making it ideally suited for studying the boosted and quasi-boosted regimes.

In this paper, we present three applications of XCone which are relevant for LHC physics in and beyond the standard model. In section 2, we study high-mass dijet resonances with isolated final state jets, showing that XCone has nearly identical performance to the popular anti-k_T algorithm [9]. In section 3, we study associated Higgs boson production, showing that XCone can resolve $H \to b\bar{b}$ decays, even when the $R_{b\bar{b}}$ angle is less than the radius parameter R, in contrast to anti-k_T. In section 4, we study the classic example of boosted top quarks, showing how XCone can simultaneously identify jets and subjets in a high multiplicity final state, achieving higher signal efficiency than a traditional fat jet strategy. These three case studies highlight the versatility of the XCone jet algorithm across a wide kinematic range and motivate the use of XCone as a viable alternative to anti-k_T.

It is worth noting that there have been other attempts to merge the resolved and boosted regimes into a single analysis, such as ref. [10] which combines different event topologies into a single search. Cone algorithms like SISCone [11] have an overlap parameter that can be adjusted to achieve some of the desired jet splitting needed to resolve substructure. More recently, the "mass jump" algorithm was introduced to avoid merging separated hard prongs [12, 13]. A key novelty of the XCone approach is that no explicit distinction is made between jets and subjets in the initial jet finding algorithm. XCone can only partially replace a dedicated substructure analysis, especially since it is well-known that a fixed radius R no longer performs well in the hyper-boosted regime (see, e.g. [14, 15]). We suspect that it will be advantageous to combine XCone jet finding with other jet substructure techniques, though we do not pursue that possibility in the present work.

Note that exclusive clustering has long been part of the jet physics toolbox, though mainly in the context of sequential recombination algorithms. Indeed, for reasons of computational efficiency, XCone uses k_T-style clustering internally as part of its jet finding procedure [1]. As shown in appendix A, exclusive k_T clustering [8] (with an R parameter) also successfully interpolates between the resolved and boosted regimes. The key difference is that k_T-style jets have irregular boundaries and non-uniform active jet areas [16, 17], while XCone jets are conical and uniform. This turns out to give XCone a performance advantage over exclusive k_T, yielding better mass resolution for boosted Higgs bosons and top quarks.

Before beginning our case studies, we briefly review the XCone jet algorithm [1]. XCone is based on minimizing the event shape N-jettiness [18] using a measure inspired by the jet shape N-subjettiness [19, 20]. A generic definition of N-jettiness is

$$\widetilde{\mathcal{T}}_N = \sum_i \min \left\{ \rho_{\text{jet}}(p_i, n_1), \ldots, \rho_{\text{jet}}(p_i, n_N), \rho_{\text{beam}}(p_i) \right\}, \tag{1.1}$$

where $n_A = \{1, \hat{n}_A\}$ are N light-like axes and p_i are the particles in the event. Based on a

jet measure $\rho_{\text{jet}}(p_i, n_A)$ and a beam measure $\rho_{\text{beam}}(p_i)$, the minimum inside of $\widetilde{\mathcal{T}}_N$ partitions the event into N jet regions and one unclustered beam region. Ideally, one would find the global minimum of $\widetilde{\mathcal{T}}_N$ over all possible axes n_A,

$$\mathcal{T}_N = \min_{n_1, n_2, \ldots, n_N} \widetilde{\mathcal{T}}_N, \tag{1.2}$$

though in practice, one uses iterative procedures to find a local $\mathcal{T}_N$ minimum starting from infrared and collinear safe seed axes. A variety of N-jettiness measures have been proposed in the literature (most especially in refs. [20, 21], see also [22, 23]), but here we stick exclusively to the XCone recommended measure, namely the conical geometric measure with $\gamma = 1$ [1]:

$$\rho_{\text{jet}}(p_i, n_A) = p_{Ti} \left(\frac{2 n_A \cdot p_i}{n_{TA} \, p_{Ti}} \frac{1}{R^2} \right)^{\beta/2} \approx p_{Ti} \left(\frac{R_{iA}}{R} \right)^{\beta},$$
$$\rho_{\text{beam}}(p_i) = p_{Ti}. \tag{1.3}$$

As recommended in ref. [1], we consider two default values for the parameter β. The XCone default is $\beta = 2$, which (approximately) aligns the jet axis with the jet momentum, as with standard cone algorithms [24]. A recoil-free default option is provided by $\beta = 1$, where the jet axis aligns with the hardest cluster in a jet [20, 25], providing enhanced robustness against jet contamination [26]. As described in ref. [1], we use a generalized k_T clustering algorithm to define seed axes for one-pass $\mathcal{T}_N$ minimization.

2 Dijet resonances and comparison to anti-k_T

For our first case study, we compare the performance of XCone to anti-k_T in the resolved regime of well-separated jets. Inclusive jet algorithms like anti-k_T identify a variable number of jets above some p_T threshold, which is useful for classifying events into different jet multiplicity bins. Exclusive jet algorithms like XCone always return a fixed number of jets N, which is useful if the number of desired jets is known in advance. For widely separated *cone* jets, however, the distinction between inclusive and exclusive cone jet algorithms is rather mild, since for typical R values, an exclusive cone jet algorithm will just return the N hardest jets from an inclusive cone jet algorithm. Since anti-k_T acts like an idealized cone algorithm for well-separated jets [9], XCone jets should be quite similar to the hardest N anti-k_T jets. When we study overlapping jets in sections 3 and 4, the inclusive/exclusive distinction will become much more important.

A good setting to study the resolved regime is a heavy resonance decay to dijets, where the two resulting jets are back-to-back and isolated. Here, we consider the scenario

$$pp \to Z' \to q\bar{q}, \tag{2.1}$$

where Z' is a heavy boson with mass $m_{Z'}$ and q is a u, d, or s quark. We start with $N = 1$ and show that XCone typically matches the hardest anti-k_T jet, up to an expected two-fold ambiguity when the jets are nearly degenerate in p_T. Going to $N = 2$, both XCone and anti-k_T can successfully reconstruct the dijet resonance peak. Even at $N = 3$, the found
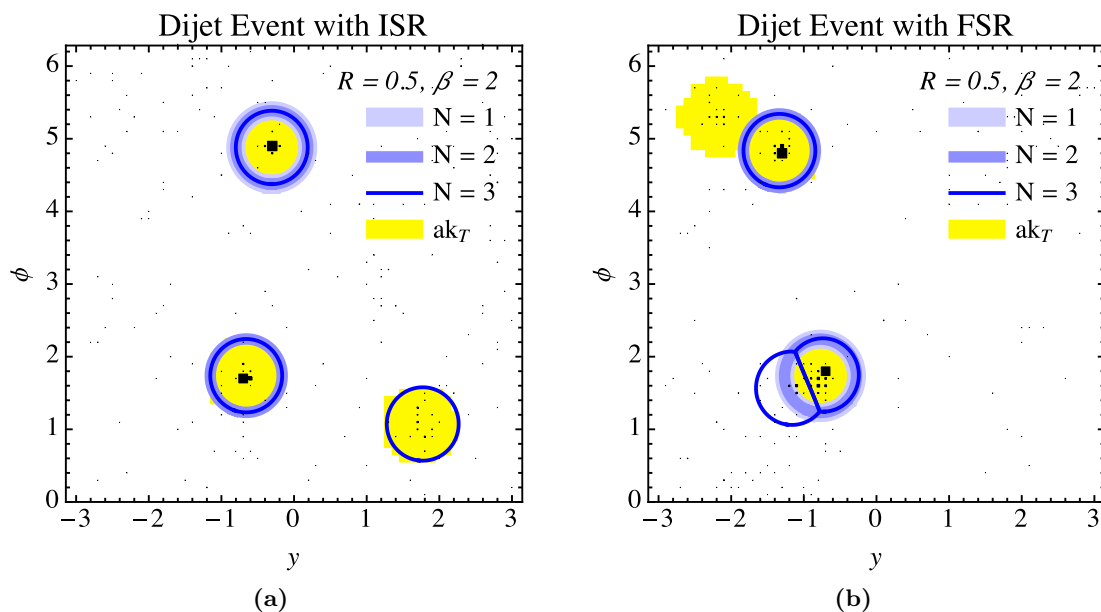
Figure 1. Example XCone jet regions found with $N = 1$, 2, and 3. These are dijet resonance events, using $R = 0.5$ and $\beta = 2$. (a) For widely separated jets, XCone and anti-k_T identify nearly identical jet regions, including an additional jet from ISR when $N = 3$. (b) XCone is able to identify jet substructure from FSR, even if the jet regions are closer than $\approx R$.

jets are quite similar for typical choices of jet parameters, though XCone will identify final state jets with substructure. Overall, XCone has essentially identical performance to anti-k_T in this basic jet reconstruction scenario for $N = 2$, but can exhibit different behavior for $N = 3$ depending on the event topology. Example XCone jet regions are shown in figure 1.

In the following study, we use Pythia 8.176 [27, 28] to simulate Z' events at the $\sqrt{s} = 14\,\text{TeV}$ LHC. We take $m_{Z'} = 1\,\text{TeV}$ and assume equal couplings to the three light quarks. All of the final-state particles (except neutrinos) with $|\eta| < 3.0$ are considered for analysis. Anti-k_T jets are found using FASTJET 3.1.2 [29] with standard E-scheme recombination. XCone jets are found using NSUBJETTINESS 2.2.0 as part of FASTJET CONTRIB [30], using the XCone default measure with $\beta = 2$ and $\beta = 1$. For all algorithms, the jet radius parameter is $R = 0.5$.

## 2.1 $N = 1$ for hardest jet

For $N = 1$, the XCone jet will tend to align with the hardest anti-k_T jet in the event. The reason is that the XCone measure in eq. (1.3) penalizes unclustered p_T by design. In figure 2a, we see that anti-k_T and XCone yield nearly identical single jet p_T spectra, with the expected structure at $m_{Z'}/2$ from a dijet resonance decay. As shown in figure 2c, there is a two-fold ϕ ambiguity in the found jets, as expected from dijet events where both jets have similar p_T values. Note that the box sizes are logarithmic in bin counts, and in the majority of cases, XCone and anti-k_T find very similar jet regions.

In figure 2b, we compare the found jet p_T on an event-by-event basis, and find a sharp peak at $\Delta p_T = p_T^{\text{anti-}k_T} - p_T^{\text{XCone}} = 0$. On a logarithmic scale, one can see a small tail
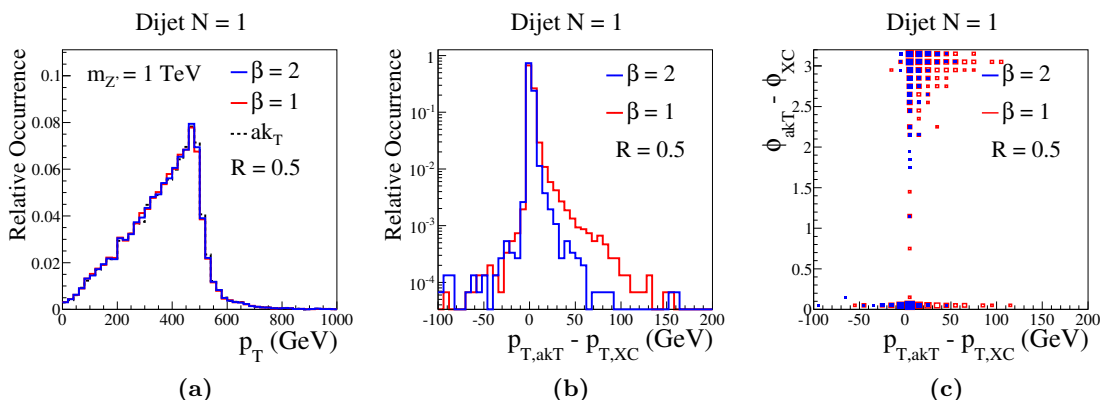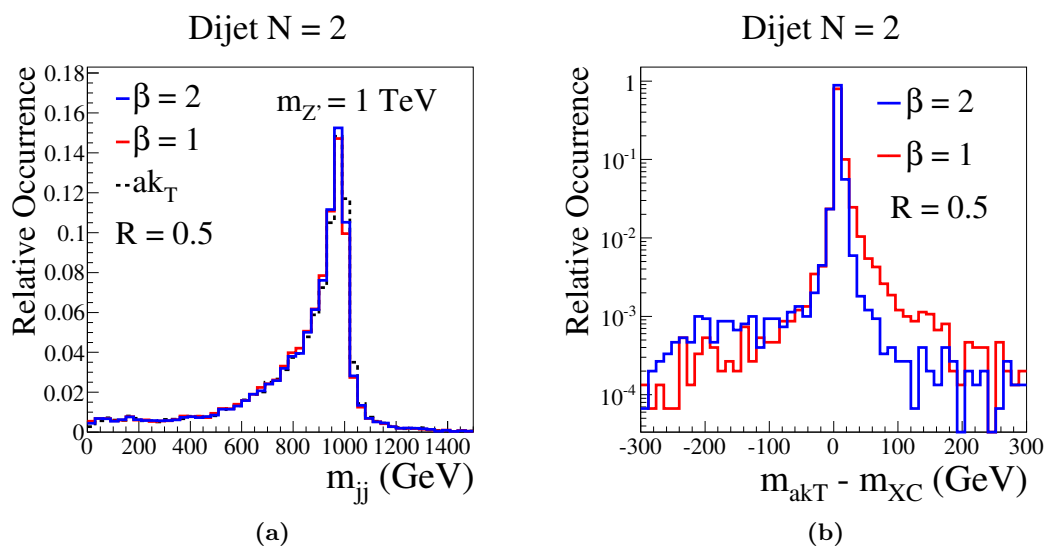
Figure 2. Single jet kinematics of $N = 1$ XCone versus the hardest anti-k_T jet, measured on the dijet resonance sample. Shown are both the XCone default ($\beta = 2$) as well as the recoil-free variant ($\beta = 1$). (a) Single jet p_T spectrum. (b) Jet p_T difference between XCone and anti-k_T jet, showing that anti-k_T jets are slightly harder on average. (c) Jet p_T difference versus azimuth difference, showing the expected two-fold $\phi \leftrightarrow \phi + \pi$ ambiguity for dijets of comparable p_T. Here and in figure 5c below, the sizes of the boxes scale logarithmically with the number of entries, with solid blue boxes for $\beta = 2$ and empty red boxes for $\beta = 1$.
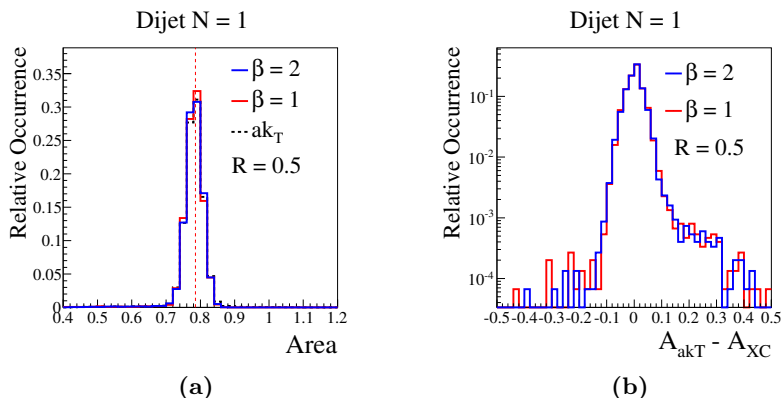
Figure 3. Same $N = 1$ comparison as figure 2. (a) Single jet areas, showing the expected peak at πR^2. (b) Jet area difference, showing that anti-k_T jets occasionally have a higher area, explaining the p_T asymmetry seen in figure 2b.

extending to $\mathcal{O}(50\,\text{GeV})$ for $\beta = 2$, with larger deviations possible in the $\beta = 1$ case. It is interesting that the Δp_T distribution is not symmetric, such that anti-k_T jets tend to have a larger p_T than XCone jets. In figure 3a, we plot the active jet area [16, 17],[1] which is quite similar between the two algorithms and peaked at the expected value of πR^2. On an event-by-event basis, though, there is a population of anti-k_T jets that are systematically larger than XCone jets, as shown in figure 3b. This occurs because anti-k_T clustering can

---

[1]We use the built-in FASTJET area determination routines using active ghosts. For the general conical measure introduced in ref. [1], the active jet area can be determined analytically, though this is not as straightforward for the conical geometric measure used here.

Figure 4. Dijet kinematics of $N = 2$ XCone versus the two hardest anti-k_T jets, measured on the dijet resonance sample. (a) Dijet mass, showing the expected peak at $m_{Z'} = 1\,\mathrm{TeV}$. (b) Dijet mass difference between XCone and anti-k_T jet, showing comparable reconstruction.

yield jets that extend beyond the conical boundary [9]. The Δp_T asymmetry then arises because these slightly bigger anti-k_T jets contain more particles.

Comparing the performance of different β values, $\beta = 2$ jets are more similar to anti-k_T jets since both methods align the jet axis with the jet momentum. The $\beta = 1$ jets are slightly softer, since they do not recoil away from the hard jet center to absorb soft radiation. In the absence of pileup, however, the $\beta = 2$ and $\beta = 1$ performance is quite similar on single jet reconstruction.[2]

## 2.2 $N = 2$ for dijet reconstruction

For dijet resonance reconstruction, $N = 2$ is the most natural choice for running an exclusive cone jet algorithm. As shown in figures 4a and 4b, both anti-k_T and XCone give a good reconstruction of the resonance peak, and they largely agree on the m_{jj} value on an event-by-event basis, without much of an asymmetry in the $m_{jj}^{\mathrm{anti-}k_T} - m_{jj}^{\mathrm{XCone}}$ distribution. XCone can therefore act as a replacement for anti-k_T for dijet resonance reconstruction, with comparable performance.[3]

2.3 $N = 3$ and ISR vs. FSR

Thus far, XCone and anti-k_T have exhibited very similar behavior, but differences start to appear when considering $N = 3$. There are two main ways to achieve three jet configurations: either there is sufficient initial state radiation (ISR) to form an additional

---

[2]In the presence of pileup, the directions of the $\beta = 1$ axes are more robust to pileup contamination [26].

[3]It is known that the $R = 0.5$ cone size is typically too small to capture all of the dijet decay products [31]. While we did find that better performance could be obtained with somewhat larger R, we wanted all of the plots in this paper to have a common cone size for ease of comparison.
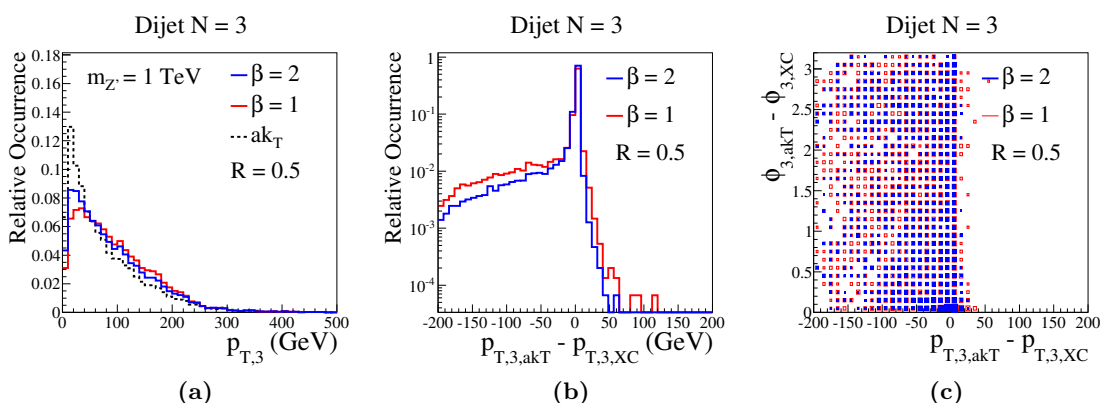
Figure 5. Comparing the third hardest jet between XCone $N = 3$ and anti-k_T, measured on the dijet resonance sample. (a) Third jet p_T spectrum. (b) Third jet p_T difference between XCone and anti-k_T, showing that XCone has a somewhat harder spectrum due to its ability to identify FSR subjets. (c) Third jet p_T difference versus azimuth difference, showing a population of events where the third jet kinematics are completely different between the algorithms. Again, the sizes of the boxes scale logarithmically with the number of entries.

widely-separated jet, or there is sufficient final state radiation (FSR) to give one of the primary jets some two-prong substructure. In the ISR case (as in figure 1a), anti-k_T and XCone still give very similar results since the jets are non-overlapping. In the FSR case (as in figure 1b), XCone will often identify two separate prongs inside a fat clover jet, whereas anti-k_T can only identify FSR if it is further away than R from the hard jet core.

From the p_T spectra in figure 5a, we see that the third jet is often softer in the anti-k_T case, as expected if anti-k_T tends to identify ISR jets. XCone, on the other hand, is able to find FSR radiation that lies close to one of the two original jets, and thus is more likely to find a hard third jet adjacent to the hard dijet structure. This is highlighted in figures 5b and 5c, which shows that the third anti-k_T jet can have completely uncorrelated kinematics from the third XCone jet. We can gain further insight in figure 6a, which shows the distance between the third jet and the closest harder jet. In the anti-k_T case, the third jet is forced to be further away than R from the jet core, whereas in XCone case, the third jet can go nearly to $\Delta R = 0$, corresponding to XCone finding substructure within a fat clover jet, as desired, instead of finding a separate ISR jet.

The same effects are visible in the area distributions in figures 6b and 6c. While the overall area distributions are not so dissimilar (particularly in the $\beta = 2$ case), on an event-by-event basis, there is a population of events where the third XCone jet has substantially smaller jet area, indicative of jet overlap. This is the flip side of the area distributions for $N = 1$ in figure 3b, where anti-k_T jets could grow larger in size by incorporating a neighboring subjet. In the XCone case, that subjet is separately identified as its own jet for $N = 3$.

Despite these differences, the overall jet reconstruction is still rather similar between XCone and anti-k_T. In tables 1a and 1b, we show the fraction of events for which the nth hardest XCone jet is within $R/2 = 0.25$ of the nth hardest anti-k_T jet. For $\beta = 2$, the three
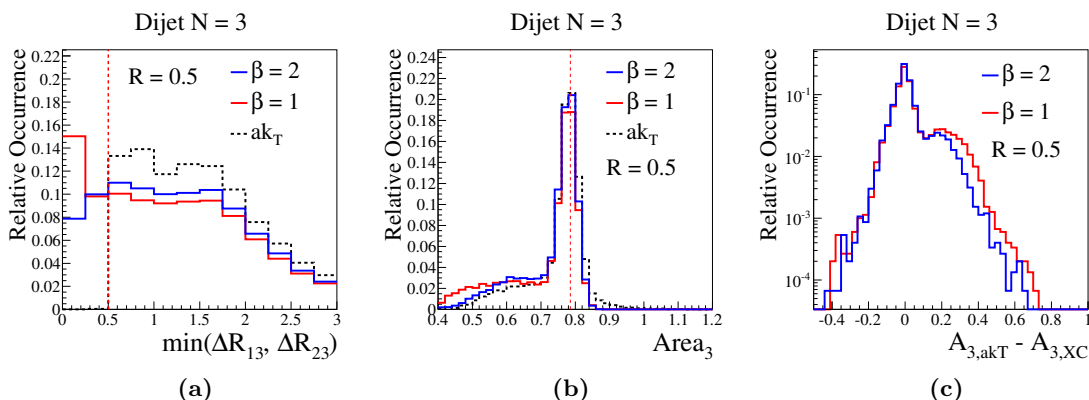
Figure 6. Same $N = 3$ comparison as figure 5. (a) Angle of the third hardest jet to the nearest harder jet, showing that XCone jets can be located as close as $\Delta R = 0$ whereas anti-k_T jets are forced to have $\Delta R > R$. (b) Third jet area distribution, showing the expected peak at πR^2, but with larger tails than in the $N = 1$ case in figure 3a. (c) Third jet area difference, showing a population of XCone jets with much smaller areas due to jet splitting.

($\beta = 2$)	XCone 1	XCone 2	XCone 3
AKT 1	0.925	0.077	0.031
AKT 2	0.075	0.913	0.042
AKT 3	0.000	0.006	0.795
AKT 4	0.000	0.001	0.043

(a)

($\beta = 1$)	XCone 1	XCone 2	XCone 3
AKT 1	0.884	0.120	0.070
AKT 2	0.116	0.870	0.076
AKT 3	0.000	0.007	0.720
AKT 4	0.000	0.001	0.041

(b)

Table 1. Comparing XCone $N = 3$ to anti-k_T. Shown is the fraction of events where the nth hardest XCone jet is within $R/2 = 0.25$ of the nth hardest anti-k_T jet. (a) The $\beta = 2$ default which behaves most similarly to anti-k_T. (b) The $\beta = 1$ recoil-free variant where larger differences are possible.

hardest jets are well aligned 80% to 90% of the time. For $\beta = 1$, there are larger deviations, though often this is just because the first and second jets are reversed in p_T ordering. We conclude that the use of XCone is particularly advantageous for tagging small-angle FSR, but otherwise will have similar performance to anti-k_T.

Of course, there may be physics contexts where splitting jets by nearest-neighbor is undesirable and circular jet regions are preferred. After all, the hardest anti-k_T jet in an event tends to be circular, whereas proximate softer jets form crescent shaped regions, and this is often a desirable feature for jet calibrations and calculations. In this context, note that XCone jet regions are fully determined by the locations of the corresponding jet axes, independent of the details of the jet constituents. Therefore, it is straightforward to test for jet splitting by simply checking whether any two jet axes are closer than $2R$. One could even imagine running XCone in a mode where N is subsequently decreased until the distances between all axis pairs are larger than $2R$, forcing circular jet regions. As we will see below, though, it is precisely the ability of XCone to split abutting jets which allows

it to handle extreme kinematic circumstances where anti-k_T reconstruction inevitability leads to jet merging.

3 Boosted Higgs bosons and intelligent jet splitting

To highlight the distinct advantages of XCone, we now consider physics situations where resolving substructure is a key element of the analysis. Because XCone always identifies N jets, it is well-suited to physics applications with a fixed number of expected (sub)jets. This is particularly interesting for cases involving jet substructure, where traditional jet algorithms yield merged fat jets, but XCone can identify jets and subjets simultaneously.

As a well-motivated example at the LHC, consider associated Higgs boson production where the Higgs decays to bottom pairs [32, 33]:

$$pp \to HZ \to b\bar{b}\nu\bar{\nu}. \tag{3.1}$$

Apart from possible ISR, the final state consists only of two b-jets. To fight QCD backgrounds, the p_T of the Higgs boson must be reasonably large [34]. However, in this regime, the Higgs decay products are more collimated, often resulting in jet merging. Roughly speaking, the two b-jets will be merged into a single fat jet when the Higgs boson is at the scale

$$p_T^{\mathrm{merge}} \simeq \frac{2m_H}{R}. \tag{3.2}$$

In order to counteract this effect, either R can be decreased until it is small enough to resolve two separate b-jets, or jet substructure techniques can be used [35].

This (quasi-)boosted Higgs analysis is well-suited for XCone. At minimum, $N = 1$ can identify a single fat jet, after which existing jet substructure techniques can be applied. Though we will not perform a detailed jet substructure analysis here, we will show that XCone with $N = 1$ has nearly the same signal efficiency as anti-k_T as a function of p_T, and therefore can be used as a suitable starting point for a full boosted Higgs analysis.

More intuitively, $N = 2$ can be used to identity the two hard b-jets in the event at all p_T scales. This $N = 2$ strategy is very similar to what is already being done in existing ATLAS and CMS studies [32, 33], where anti-k_T is used to resolve two separate b-jets. For anti-k_T, the b-jets merge at high enough p_T, so this resolved technique is no longer efficient (see [36] for a recent discussion). For XCone, we show that the corresponding $N = 2$ resolved strategy can be pushed deep into the high p_T regime while maintaining good signal efficiency. For this reason, we advocate XCone as a promising approach to extrapolate resolved analyses into the boosted regime.

Example event displays using the $N = 1$ and $N = 2$ methods are shown in figure 7. In the text, we restrict our comparisons to anti-k_T, though in appendix A.1, we also show results for exclusive k_T, which has performance comparable to XCone, albeit with irregular jet boundaries. A full accounting of background processes is beyond the scope of this work, though we do perform a sanity check in appendix B to verify that XCone does not unnecessarily sculpt the $Z + \mathrm{jets}$ background. Since the relative performance of the boosted and resolved strategies depends on the details of the background, we postpone a direct comparison of $N = 1$ with $N = 2$ to future work.
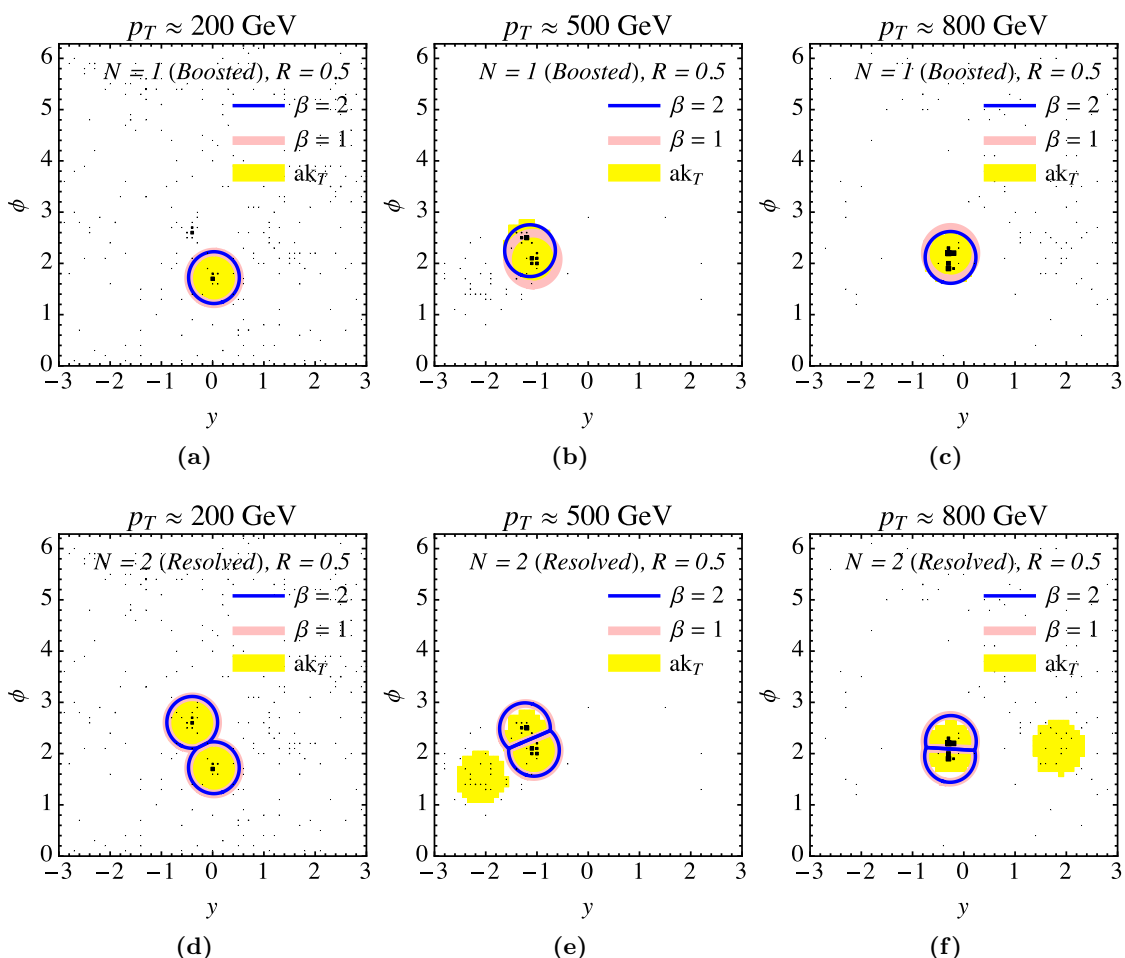
Figure 7. Example XCone jet regions for the Higgs analysis for $p_T \approx \{200, 500, 800\}$ GeV, using $R = 0.5$. Top row: a boosted Higgs analysis with $N = 1$, where XCone and anti-k_T identify nearly the same jet regions. Bottom row: a resolved Higgs analysis with $N = 2$, where XCone separately identifies the $H \to b\bar{b}$ substructure while anti-k_T often identifies ISR. For each p_T value, the same event appears for $N = 1$ and $N = 2$.

Like the previous dijet study, we use Pythia 8.176 [27, 28] at the $\sqrt{s} = 14$ TeV LHC to simulate $pp \to HZ$. For simplicity, we force the decays $Z \to \nu\bar{\nu}$ and $H \to b\bar{b}$. Like in the previous study, all of the final-state particles (except neutrinos) with $|\eta| < 3.0$ are considered for analysis. In order to analyze the properties of the algorithm in different p_T regimes, we place generator-level p_T cuts on the Higgs boson between 200 and 1000 GeV. We use the same $R = 0.5$ jet radius for all analyses in this section, such that $p_T^{\mathrm{merge}} \simeq 500$ GeV is in the middle of our studied p_T range.

3.1 $N = 1$ for boosted analysis

Since the pioneering work in ref. [35], the boosted Higgs channel has often been been analyzed by finding one fat jet with a large radius parameter, and then using substructure techniques to analyze its properties (see e.g. [37]). Here, we compare $N = 1$ XCone to

anti-k_T to show that they give similar behavior in the boosted regime, though we stick to a relatively small $R = 0.5$.[4]

Unlike in the dijet resonance study, the difference between $\beta = 1$ and $\beta = 2$ is more noticeable for quasi-boosted Higgs bosons. As described in refs. [20, 25], $\beta = 1$ minimization aligns the jet axis with the hardest cluster within a jet, whereas $\beta = 2$ minimization places the jet axis approximately in the direction of the jet momentum. Roughly speaking, $\beta = 1$ finds the "median" jet axis direction whereas $\beta = 2$ finds the "mean" jet axis direction. For the boosted Higgs case, the $\beta = 1$ jet is more likely to point in the direction of one of the two b-jets, while the $\beta = 2$ jet is more likely to lie in between the two b-jets and track the Higgs momentum direction. Anti-k_T (with standard E-scheme recombination [41]) acts like $\beta = 2$ since it also aligns the jet axis with the jet momentum.

In the top row of figure 8, we show the single jet invariant mass as the minimum Higgs p_T (at generator level) is adjusted from $200\,\mathrm{GeV}$ to $500\,\mathrm{GeV}$ to $800\,\mathrm{GeV}$. With increasing p_T, more of the Higgs decay products are contained inside a single jet and the peak at $m_j = 125\,\mathrm{GeV}$ grows. By eye, the anti-k_T and $\beta = 2$ distributions are quite similar, whereas the $\beta = 1$ case has a somewhat worse performance since the jet axis is misaligned from the Higgs boson momentum. Though not shown in the plot, the default conical geometric XCone measure [1] yields a slightly better Higgs peak than the original conical measure [20]. In the bottom row of figure 8, we show the distribution of active jet areas, where both algorithms have a peak at πR^2, though anti-k_T has a slight high-side tail when $p_T \simeq p_T^{\mathrm{merge}}$.

We quantify the Higgs reconstruction efficiency in figure 9, which shows the fraction of jets in the Higgs mass window $m_j \in [100, 150]\,\mathrm{GeV}$. At very high p_T values, the algorithms have very similar performance, but $\beta = 2$ does better in the vicinity of p_T^{merge}. This is because the $\beta = 2$ jet axis is more likely to lie in between the two b-jets, so the jet is more likely to capture the full Higgs decay products. As expected, anti-k_T and $\beta = 2$ are very similar.

3.2 $N = 2$ for resolved analysis

For this Higgs production scenario, the real power of XCone comes from using $N = 2$. In the unboosted regime, the standard analysis strategy is to find two b-jets, reconstruct their invariant mass, and look for a peak at the known Higgs mass [32, 33]. In the boosted regime with jet merging, though, algorithms like anti-k_T are likely to find one fat Higgs jet and one ISR jet elsewhere in the event, so a dijet reconstruction strategy is no longer effective. By contrast, since XCone is an exclusive cone algorithm, it will always identify two jets regardless of the Higgs p_T. To find boosted Higgs bosons with XCone, we can simply run with $N = 2$ and perform a standard resolved jet analysis.

In the top row of figure 10, we show the reconstructed dijet invariant mass comparing XCone with anti-k_T. For low Higgs p_T, all algorithms find the Higgs peak with roughly

---

[4]The original BDRS paper used the Cambridge/Aachen algorithm [38–40] to identify this fat jet. To avoid a proliferation of curves, we only compare XCone to anti-k_T in our analysis. Regardless of the fat jet starting point, one can still recluster with Cambridge/Aachen to apply the BDRS mass drop criteria.
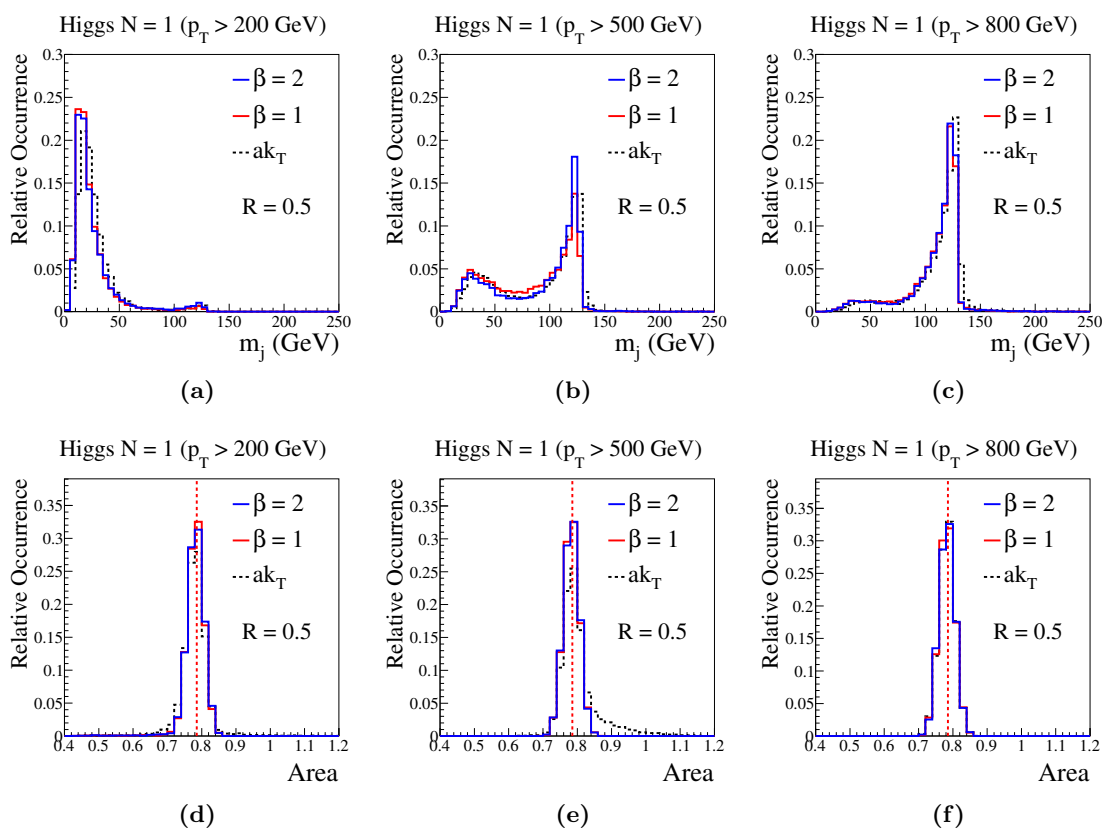
Figure 8. Top row: comparing boosted Higgs reconstruction between XCone with $N = 1$ and the hardest anti-k_T jet, using $R = 0.5$. As the Higgs p_T increases from (a) 200 GeV to (b) 500 GeV to (c) 800 GeV, both methods capture the merged Higgs decay products, yielding a growing mass peak at $m_H = 125$ GeV. Bottom row: comparing Higgs jet area using XCone $N = 1$ and the hardest anti-k_T jet. All distributions show the large expected peak at $A = \pi(0.5)^2$.

the same line shape.[5] As the Higgs p_T increases, the anti-k_T distributions move to higher dijet masses because of a merged Higgs jet being paired with an ISR jet, whereas XCone maintains good performance regardless of p_T. In the bottom row of figure 10, we show the jet area distributions. Anti-k_T jets peak at πR^2 regardless of the Higgs p_T, whereas XCone jets transition from πR^2 at low p_T to roughly half that at high p_T, indicative of the desired split jet regions.

We show the Higgs reconstruction efficiency in figure 11a as a function of the Higgs p_T. Anti-k_T jets start to merge around $p_T = 300$ GeV and the Higgs efficiency drops significantly. XCone has nearly flat efficiency as a function of Higgs p_T, even as the p_T crosses beyond the p_T^{merge} scale. At higher p_T values, the $\beta = 2$ jets see a performance degradation, since the $\beta = 2$ jets are more influenced by ISR at wide angles. The $\beta = 1$ jets are able to maintain their performance since the jet axes tend to always align with the momentum of the Higgs decay products. Overall, the XCone reconstruction efficiency is around 65% for $R = 0.5$.

---

[5]The low mass tail in each of the plots can be explained by neutrinos from B meson decays within the b-jet.
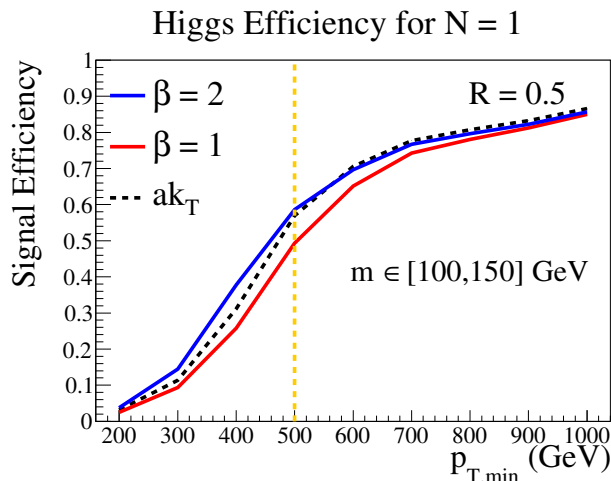
Figure 9. Efficiency for $N = 1$ boosted Higgs reconstruction as a function of Higgs p_T, with the mass window $m_j \in [100, 150]$ GeV. The efficiency grows when the p_T is above the merging scale $2m_H/R$. XCone $\beta = 2$ outperforms $\beta = 1$ in the transition region since the former centers the jet along the Higgs momentum.

3.3 $N = 3$ for ISR vetoing

To improve the XCone performance, we have to account for ISR, which is the leading cause of misreconstruction. In the presence of hard ISR, XCone can identify an ISR jet instead of finding one of the two b jets. To address this issue, we can explicitly identify the ISR jet using $N = 3$ and find the best reconstruction among the $N = 2$ and $N = 3$ options.[6]

We first run XCone with $N = 2$ and check whether the dijet mass is in the $m_{jj} \in [100, 150]$ GeV window. If not, we run XCone with $N = 3$ and apply the Higgs mass test on the pair of jets with the smallest invariant mass, as these are kinematically the most likely candidates to be the Higgs decay products. Allowing two pathways for Higgs reconstruction gives improved signal efficiency, and in figure 11b, we see that both $\beta = 1$ and $\beta = 2$ now have efficiencies around 75%. Applying the same 2- and 3-jet technique to anti-k_T does improve the signal efficiency somewhat, though XCone still has better performance for $p_T \gtrsim 300$ GeV.

We conclude that XCone is highly efficient in reconstructing Higgs bosons across a range of kinematics, from the resolved to quasi-boosted to boosted regimes. Comparing figure 9 with figure 11, we see that $N = 1$ does yield better signal efficiency at very high boosts, whereas $N = 2, 3$ yields uniform (and still quite good) performance. Ultimately, one may want to combine all three methods, although this would require a full understanding of background processes (see discussion in appendix B). In a full analysis, one would also want to exploit b-tagging to better identify the Higgs candidate and mitigate non-b backgrounds. This is especially important when using the combined $N = 2, 3$ method, where background events have two pathways to land in the signal window. But the main take away from this

---

[6]An alternative approach is to use a modified beam measure (such as the $\gamma = 2$ option discussed in ref. [1]) to preferentially select central jets.
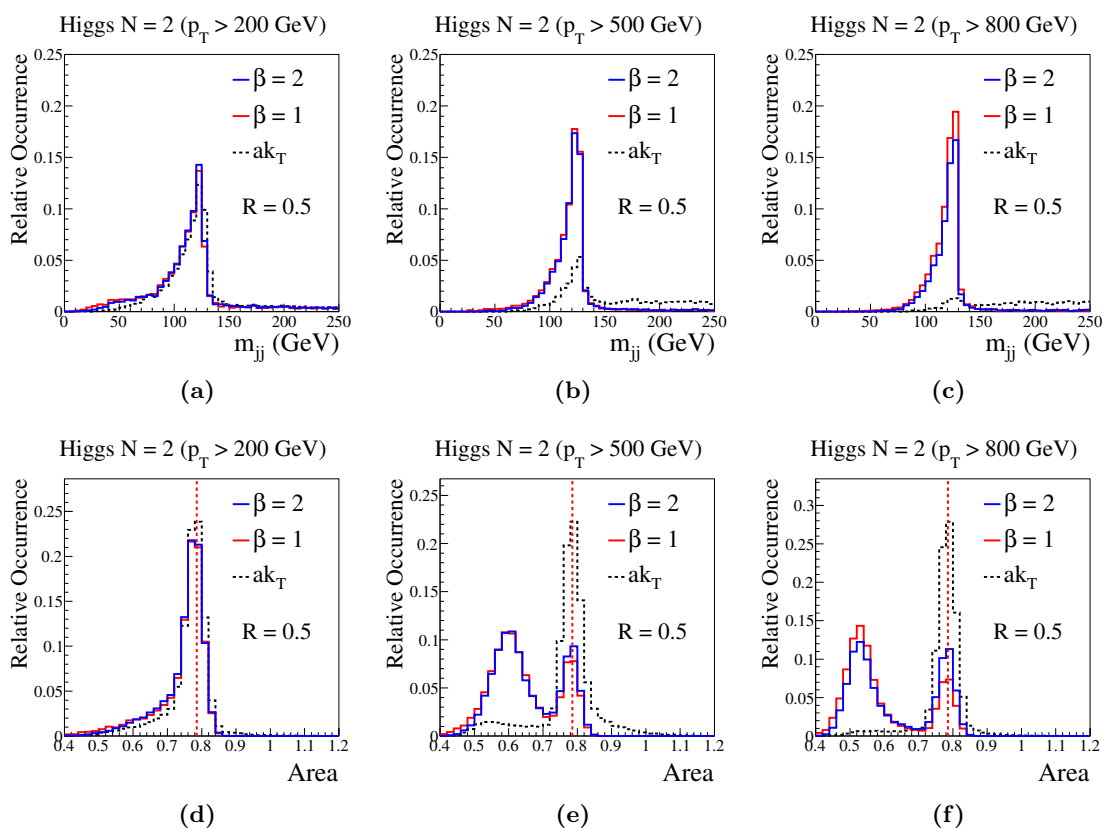
Figure 10. Same as figure 8 but for $N = 2$. As the Higgs p_T increases from (a) 200 GeV to (b) 500 GeV to (c) 800 GeV, anti-k_T suffers from jet merging, whereas XCone yields a dijet Higgs peak across the p_T spectrum. At low p_T, both distributions have the expected area peak at $A = \pi(0.5)^2$. As p_T increases, the XCone area falls to roughly half its original value, indicative of overlapping jets. See figure 18 for a comparison to exclusive k_T.

study is that XCone allows traditional resolved analyses to be extended into the boosted regime, providing a p_T-independent method for Higgs reconstruction.

4 Boosted top quarks and high-multiplicity final states

Given the success of XCone in reconstructing boosted Higgs bosons, we now test whether XCone can handle the increasingly complex final states possible at LHC collision energies. An important process at the LHC is pair production of top quarks with fully hadronic decays:

$$pp \rightarrow t\bar{t}, \qquad t \rightarrow Wb \rightarrow q\bar{q}'b. \tag{4.1}$$

At low $m_{t\bar{t}}$, the final state consists of six resolved jets. At high $m_{t\bar{t}}$, the jets are arranged into two fat jets with three-prong substructure, and a variety of substructure techniques have been developed to tag these boosted tops (see, e.g. [42–45]). Here, we show that XCone with $N = 6$ can identify each of the six individual (sub)jets, regardless of the $m_{t\bar{t}}$ value, allowing the same analysis strategy to be effective in both the resolved and boosted
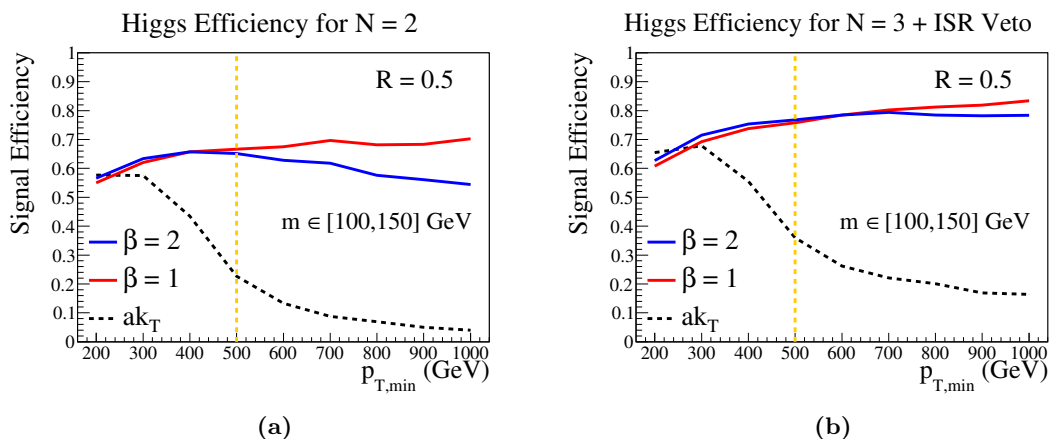
Figure 11. (a) Efficiency for $N = 2$ resolved dijet Higgs reconstruction as a function of Higgs p_T, with the mass window $m_j \in [100, 150]$ GeV. We see a degradation in the efficiency of the anti-k_T spectrum at higher p_T due to jet merging, while XCone produces constant efficiency across the spectrum at around 65%. Here, $\beta = 1$ outperforms $\beta = 2$, since the former is less susceptible to wide-angle jet contamination. (b) Same as figure 11a, but now allowing the Higgs to be reconstructed with either $N = 2$ or $N = 3$, using the minimum pairwise mass to veto ISR. Now, XCone $\beta = 1$ and $\beta = 2$ have comparable performance at around 75%. See figure 19 for a comparison to exclusive k_T.

regimes (see appendix A.2 for similar behavior from exclusive k_T). We also show a more efficient $N = 2 \times 3$ method where the event is first partitioned into hemispheres using $N = 2$ and then separated into subjets by applying $N = 3$ in each hemisphere.

Our study is based on the BOOST 2010 events samples [2], which were generated for the 7 TeV LHC.[7] For the boosted top signal, we use the Herwig $t\bar{t} \rightarrow$ hadrons samples where the generator-level top p_T ranges from 200–800 GeV in bins of 100 GeV. We also apply XCone to the Herwig dijet background sample in the same p_T bins. As in the boosted Higgs study, we take $R = 0.5$. When comparing to traditional fat jet studies, we use anti-k_T jets with $R = 1.0$ as recommended in the BOOST 2010 report [2]. For brevity, we do not include a straight $N = 2$ fat jet study for XCone, since the results are similar to those found in section 2. Example event displays from XCone are shown in figures 12 and 13.

At the outset, we want to emphasize that XCone is able to handle partially overlapping jets, as expected in the quasi-boosted regime. In the highly boosted limit, however, the subjets are fully overlapping, so substructure methods based on fat jets are typically more effective at signal/background separation. While it is possible to combine XCone with jet shapes like N-subjettiness [19, 20] for improved performance in the highly boosted limit, we find in preliminary studies that there is no real advantage to using $N = 6$ over a more traditional fat jet analysis with $N = 2$. The key advantage of XCone is that it yields

---

[7]While the BOOST 2011 report [3] included updated benchmark samples, those event files were lost due to "spring cleaning" at the host servers. Instead of generating fresh boosted top samples at 14 TeV collision energies, we have decided to use the BOOST 2010 event samples to enable easier comparisons and verifications of our results.
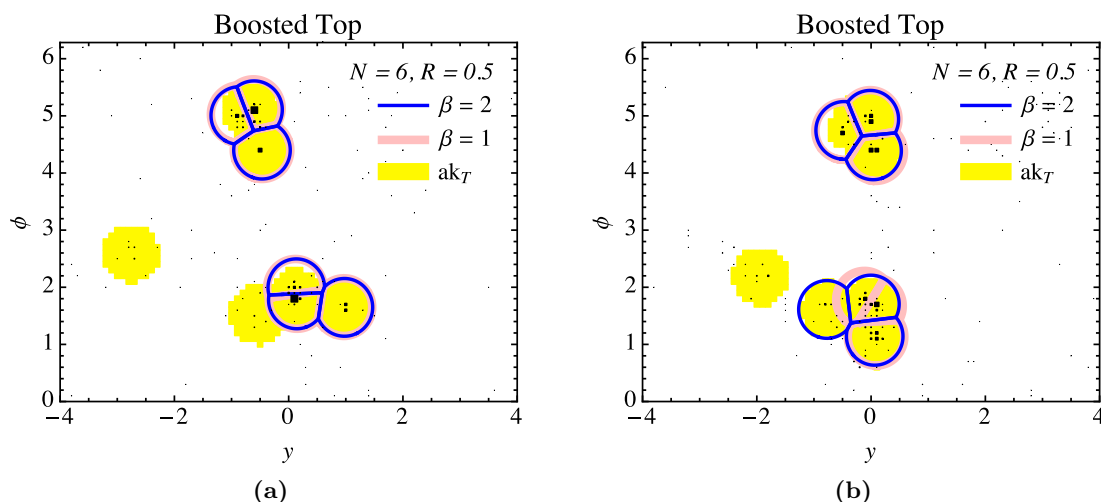
Figure 12. Two reconstructed events from the BOOST 2010 top sample, using XCone with $N = 6$ and $R = 0.5$. As is often the case, $N = 6$ and $N = 2 \times 3$ give identical results for these events. Compared to anti-k_T, XCone directly identifies three prong substructure through the initial jet finding. While $\beta = 2$ and $\beta = 1$ often give similar jet regions, they can differ more substantially, as shown on the right.
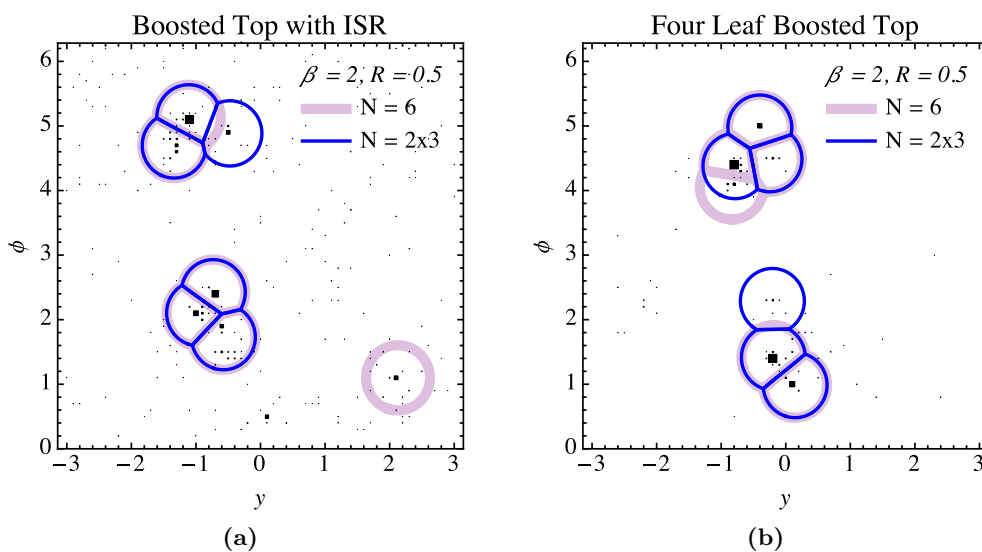
Figure 13. Pathological $N = 6$ reconstructions that are improved by using $N = 2 \times 3$. For these hand selected events, $N = 2 \times 3$ correctly identifies the boosted tops, while $N = 6$ identifies (a) an additional hard jet from ISR and (b) a fourth leaf in one of the boosted tops. Not shown are examples where the $N = 2 \times 3$ method finds an ISR jet, which can sometimes be resolved using $N = 2 \times 4$ or $N = 7$.

relatively uniform performance over a broad p_T range, and while specialized techniques can achieve better performance at extreme kinematics, XCone allows resolved techniques to be applied even when jets are overlapping.

4.1 $N = 6$ baseline analysis

The most straightforward application of XCone for hadronic tops is using $N = 6$ to resolve six jets. Like in section 3.3, one can try to improve the performance by explicitly identifying ISR jets using $N = 7$, but we find that the $N = 2 \times 3$ method shown below is more effective at dealing with the combinatorial complexity of this final state. For these studies, we have not incorporated b-tagging information, though it would be straightforward to use XCone in conjunction with recent subjet b-tagging methods [46, 47].

After running XCone with $N = 6$, we want to partition the jets into two top candidates in a way that is p_T-independent. We do this by finding all $_6C_3 = 20$ ways of partitioning the jets into two three-jet clusters, and then finding the configuration that minimizes the scalar sum of the three-jet masses. Much like in the boosted Higgs case, we expect that minimizing the mass is most likely to yield the correct top candidates. For an apples-to-apples comparison, we apply the same analysis strategy on the six hardest anti-k_T jets. In a more sophisticated analysis, one could use a χ^2-minimization approach to find the best top candidates, also incorporating W-mass and b-tagging information.

In figure 14a, we show the reconstructed top jet mass in the $p_T \in [400, 500]\,\text{GeV}$ bin, comparing XCone and anti-k_T with $N = 6$. The XCone distributions show a better resolved top peak, which is more symmetric around the top mass and has a substantially reduced high-mass tail. In the area distributions in figure 14b, we see that XCone jets are peaked at roughly $(2/3)\pi R^2$, where the factor of $2/3$ is expected since the jets are arranged in a clover configuration around the boosted top direction. The anti-k_T jets are peaked around πR^2, as expected since anti-k_T jets do not typically overlap. Because of subjet mergers, the six found anti-k_T jets are not all associated with the top quarks, leading to large invariant mass values from ISR jets.

The equivalent dijet background distributions are shown in figures 14c and 14d. In the absence of genuine three-prong substructure, the XCone jets tend to be scattered throughout the event, leading to large reconstructed invariant masses and πR^2 areas. The effect is even stronger in the anti-k_T jets, since they avoid overlaps. There is a noticeable difference between the $\beta = 1$ and $\beta = 2$ QCD dijet distributions, indicating that the mean versus median effects described in section 3.1 are significant for quark and gluon jets without well-defined substructure (a feature exploited in ref. [48]).

To define the top signal region, we take a top mass window of $m_{jjj} \in [150, 200]\,\text{GeV}$.[8] We also apply a W-tagging cut as described in the CMS analysis [49], by analyzing each pairwise combination of the three subjets and requiring a minimum pairwise invariant mass cut of $m_{jj,\text{min}} > 50\,\text{GeV}$. In figures 15a and 15b we show the efficiency and mistag rates for the top and dijet samples as a function of (generator-level) p_T. XCone has a signal efficiency of around 60% across the entire p_T range, showing the desired scale invariance. While anti-k_T starts with the same 60% efficiency in the resolved regime, the efficiency drops considerably with p_T due to jet merging, analogous to what was found in section 3.2.

---

[8]Compared to the typical mass ranges used in the BOOST 2010 report [2], this range is smaller and more symmetric. Because the peak from XCone is more narrow and symmetric around the top mass, we can use this tighter mass window without much loss in signal efficiency.

Top N = 6 ($p_T \in [400, 500]$ GeV)

Top N = 6 ($p_T \in [400, 500]$ GeV)

QCD N = 6 ($p_T \in [400, 500]$ GeV)
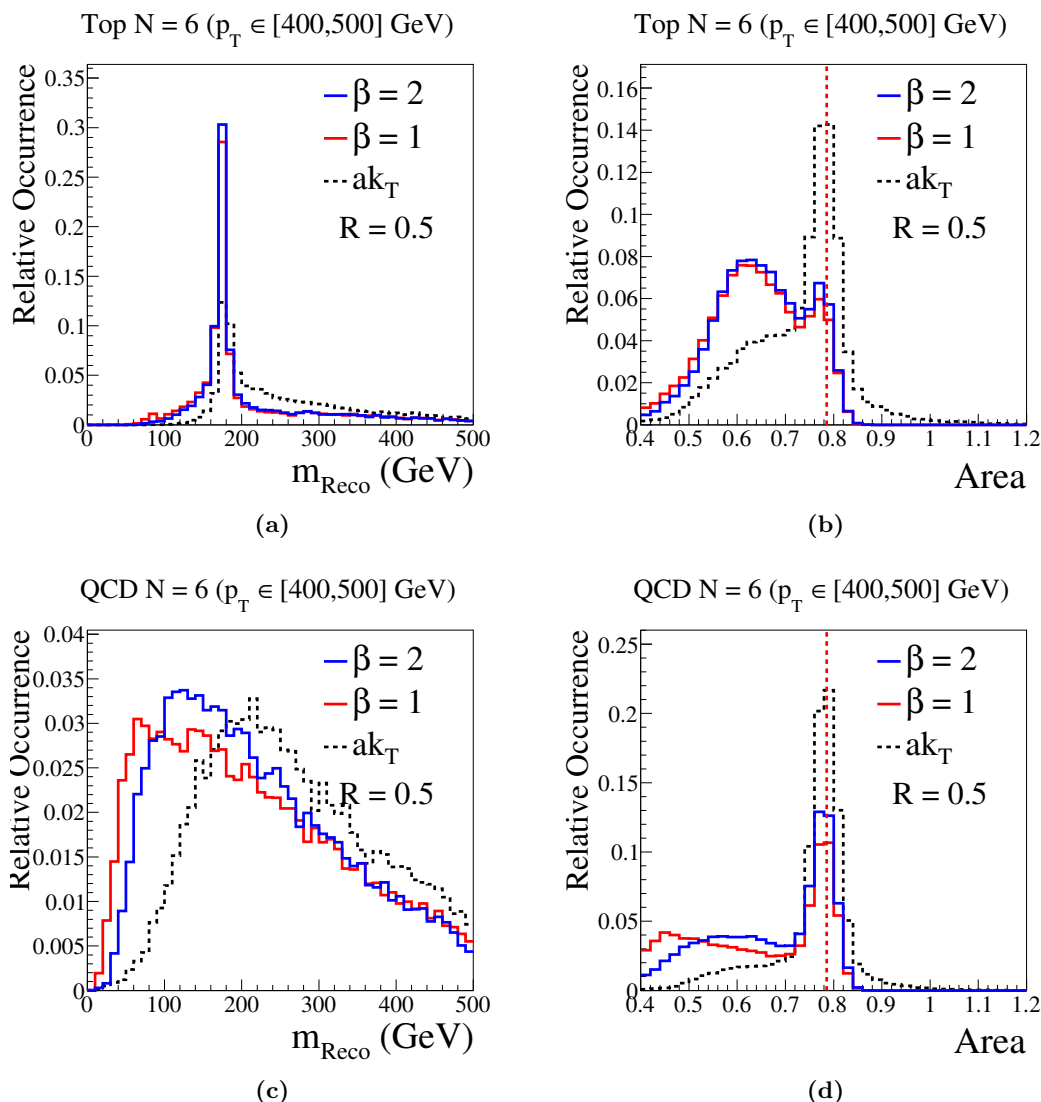
QCD N = 6 ($p_T \in [400, 500]$ GeV)

Figure 14. Top row: comparing resolved three-jet top reconstruction between XCone with $N = 6$ and the six hardest anti-k_T jets, in the $p_T \in [400, 500]$ GeV bin. Here, top candidates are identified by minimizing the sum of the three-jet masses. (a) Candidate top mass distributions, showing that XCone does not have as pronounced of a high mass tail due to ISR. (b) Area of all six jets, showing a peak at $(2/3)\pi R^2$ for XCone expected of clover jet configuration compared to a peak at πR^2 for anti-k_T expected of separated jets. Bottom row: same for the QCD background. See figure 20 for a comparison to exclusive k_T.

Both methods have around a 10% background mistag rate, which is relatively stable as a function of p_T.

The improvement in signal significance ($S/\sqrt{B}$) is shown in figure 15c, where we see that the performance remains relatively flat across the entire p_T range, with performance comparable to or better than anti-k_T. Note that we have not included b-tagging information nor additional jet shape information, so background rejection factors can be much larger in practice. From this study, we see that a simple application of XCone allows for a p_T-independent analysis strategy even for complicated final states.
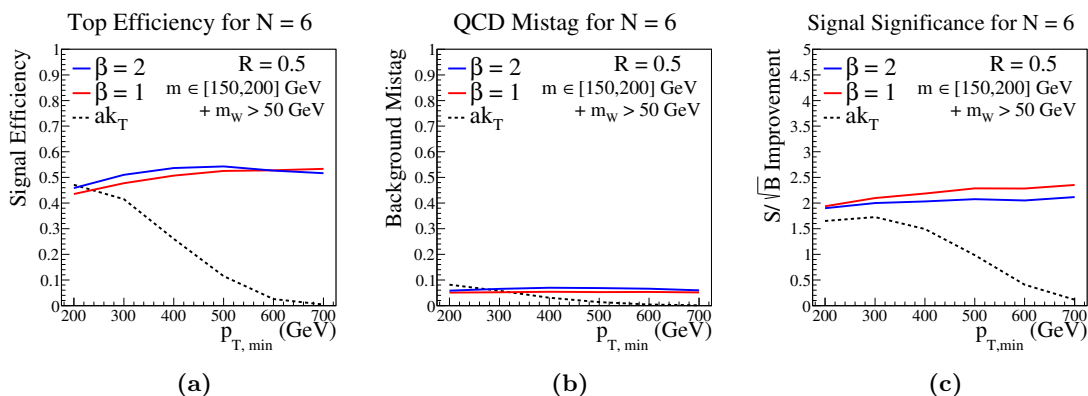
Figure 15. Comparing boosted top and XCone performance with $N = 6$ as a function of top p_T for (a) signal efficiency, (b) background mistag, and (c) signal significance gain. By avoiding jet mergers, XCone has improved performance compared to anti-k_T across the entire p_T range. See figure 21 for a comparison to exclusive k_T.

4.2 $N = 2 \times 3$ improved analysis

To further improve on the performance of XCone, we can take into account the event topology. Even with a moderate boost, the top decay products tend to arrange themselves into two hemispheres, a feature that is exploited, for example, in the HEPTogTagger [50] (see also [51]).Thus, we can use XCone in multiple stages, first dividing the event into separate top candidate regions with $N = 2$ and $R \to \infty$, and then finding jets in each of those regions using $N = 3$ and $R = 0.5$.[9]

There are two advantages of this $N = 2 \times 3$ approach over the $N = 6$ approach. First, it reduces combinatorial confusion and increases computational efficiency. Second, it ensures that each top candidate has the potential to involve three jets. Even without ISR (as in figure 13a), the $N = 6$ method can yield one four-leaf top clover and one two-leaf top clover (as in figure 13b), something that is avoided with $N = 2 \times 3$. While it is possible to get even higher signal efficiencies by applying $N = 2 \times 4$ and vetoing ISR jets (analogous to section 3.3), such an approach tends to also increase the background mistag rate, so we will not show $N = 2 \times 4$ results here.

We can compare XCone to traditional top reconstruction methods in two different ways. For a traditional boosted strategy ("Bst"), we can run anti-k_T with $R = 1.0$ to find two fat jets and then run exclusive k_T with $N = 3$ and $R = 0.5$ on the fat jet constituents to identify subjets. For a traditional resolved strategy ("Res"), we can run exclusive k_T with $N = 2$ and $R \to \infty$ to find hemisphere regions, and then run anti-k_T with $R = 0.5$ to find the three hardest jets in each hemisphere. As we will see, XCone $N = 2 \times 3$ effectively interpolates between these behaviors as a function of p_T, reproducing (and sometimes surpassing) the best performance of the traditional strategies in their respective domains. To highlight the advantages of XCone, we will be working in the regime of high signal acceptance; in the regime of high background rejection, it is well known that anti-k_T-based boosted strategies are highly effective when combined with jet substructure methods.

---

[9]For a theoretical analysis of the top mass using a related hemisphere approach, see refs. [52, 53].
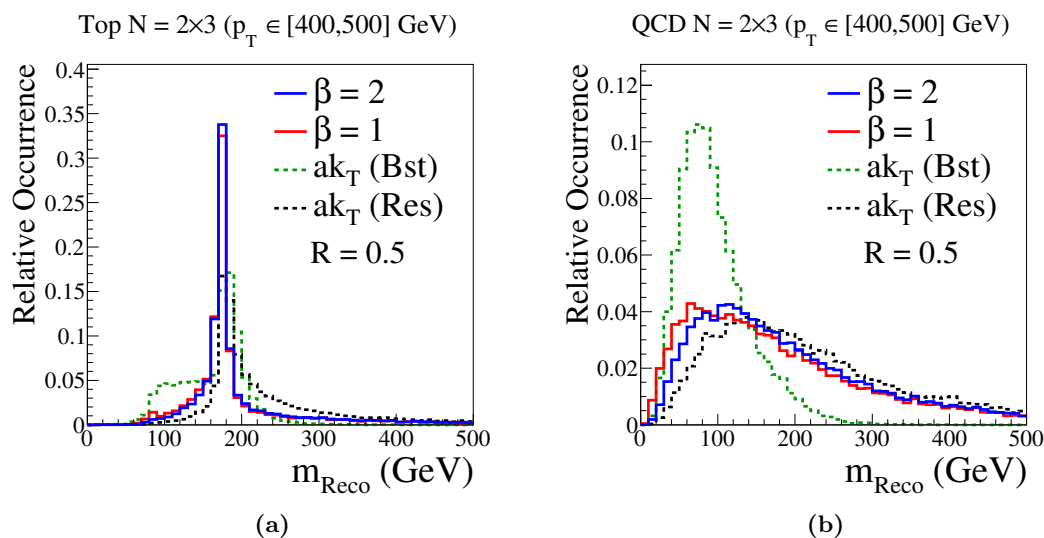
Figure 16. Reconstructed mass distributions with the $N = 2 \times 3$ strategy, for (a) top signal events and (b) QCD background events. Here we compare the XCone $N = 2 \times 3$ method to two traditional methods: a boosted strategy ("Bst") where two anti-k_T $R = 1.0$ jets have three exclusive k_T subjets, and a resolved strategy ("Res") where two exclusive k_T hemispheres have three anti-k_T $R = 0.5$ jets.

The resulting top mass distributions are shown in figure 16a, again in the $p_T \in [400, 500]$ GeV bin. The top mass distribution for XCone $N = 2 \times 3$ jets is similar to the $N = 6$ case, continuing to maintain a peaked, symmetric shape around the top mass. Crucially, $N = 2 \times 3$ reduces the high-mass tail since there are more correctly reconstructed top quarks. The traditional boosted strategy results in a W shelf caused by the $R = 1.0$ jet radius not containing the full top decay products, while the traditional resolved strategy has a high-side mass tail from the inclusion of ISR jets. XCone avoids both of these pitfalls, giving an excellent overall reconstruction.

Similarly, as shown in figure 16b, the background mass distribution for XCone falls in between the traditional boosted and resolved strategies. Like in the $N = 6$ case, both $N = 2 \times 3$ XCone jets and traditional resolved jets tend to be scattered throughout the hemisphere, leading to large invariant masses. However, the additional hemisphere constraint from using $N = 2 \times 3$ helps to control this effect, giving smaller masses on average for $N = 2 \times 3$ than $N = 6$.

The signal efficiency and background mistag rates are given in figures 17a and 17b, again for the $m_{jjj} \in [150, 200]$ GeV top mass window and $m_{jj,\text{min}} > 50$ GeV W mass cut. For the signal efficiency, it is clear the XCone interpolates between the good traditional resolved performance at low p_T and the good traditional boosted performance at high p_T, yielding approximately a 60% reconstruction efficiency throughout the p_T range. For the background mistag rate, XCone holds steady at 10%, where again, further improvements are possible using b-tagging or substructure information.

The improvement in signal significance ($S/\sqrt{B}$) is shown in figure 17c, where across the whole p_T range, the performance of XCone matches or surpasses that of the traditional
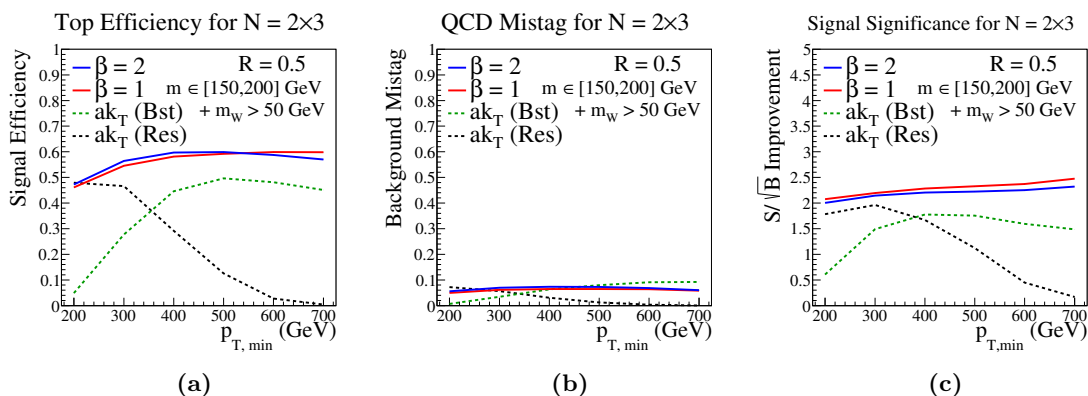
Figure 17. Comparing boosted top and XCone performance with $N = 2 \times 3$ as a function of top p_T for (a) signal efficiency, (b) background mistag, and (c) signal significance gain. XCone interpolates between the traditional resolved strategy at low p_T and the traditional boosted strategy at high p_T, with improved performance in the boosted regime due to the addition of soft subjets (at moderate p_T) and grooming away of jet contamination (at higher p_T).

boosted and resolved strategies. In the boosted regime, the improvement of XCone over traditional methods is due to two different effects already alluded to above. At moderate p_T, XCone can identify soft subjets that fall outside of the normal anti-k_T cluster radius (see also ref. [54]), increasing the jet mass into the top window. At high p_T, $R = 0.5$ acts similarly to the subjet radius in filtering [35] or trimming [55], removing jet contamination and decreasing the jet mass into the top window. We conclude that XCone gives a powerful way to extend conventional resolved analysis strategies into the boosted regime, especially if the goal is obtaining high signal efficiency.

5 Conclusions

In this paper, we presented three case studies to show how XCone can be used in a range of LHC analyses, producing comparable or better results than conventional methods. Remarkably, a single benchmark cone size of $R = 0.5$ was able to successfully reconstruct dijet resonances, boosted Higgs bosons, and boosted top quarks. We are particularly encouraged by XCone's ability to smoothly interpolate between the resolved and boosted regimes, and we anticipate that further improvement will be possible by combining XCone jet finding with additional jet substructure discriminants.

The focus of this paper has been on the physics applications of XCone, but it is also important to note the relative computational efficiency of XCone compared to other algorithms. In the case of boosted tops with $N = 6$, we find that the anti-k_T algorithm runs at an average speed of 0.3 ms per event on a typical laptop, while XCone takes around 7.3 ms per event, which is roughly 25 times slower, though still relatively fast. If computational speed is a priority, one can use XCone with the seed axes directly as the jet axes (i.e. no minimization step), which is dubbed "PseudoXCone" in the NSUBJETTINESS contrib. This takes around 0.7 ms per event, only 2.3 times slower than anti-k_T. As shown

in the companion paper, 95% of the seed axes are located at or near the global N-jettiness minimum [1], so the effectiveness of PseudoXCone is comparable to that of XCone. As an example, there are only percent-level differences in the boosted top signal significance by using PseudoXCone instead of XCone.

Beyond the examples shown in this paper, XCone should also work well in even more complex final states, including multi-jet searches for physics beyond the standard model. A key challenge for any exclusive approach is how to best veto ISR jets, and it may be that multiple N values will be needed reach optimal performance. One intriguing possibility for new physics searches is consider different N-jettiness beam measures. In particular, the conical geometric measure in ref. [1] has a $\gamma = 2$ option (compared to the recommended $\gamma = 1$ default), which preferentially select jets in the central region. This would help not only to veto ISR jets but also to control QCD backgrounds.

In an experimental context, a key practical question is how to calibrate the energy scale of XCone jets. For widely separated jets, we have seen that XCone jets are essentially the same as anti-k_T jets, so existing calibration strategies should be straightforward to adapt to XCone. The case of overlapping jets is more complicated in XCone, since jet regions can have varying shapes and sizes. As already mentioned, though, XCone jet regions are fully determined by the location of the jet axes, independent of the details of the jet constituents, so one could develop a calibration strategy that accounts for, say, the active jet area [16, 17] when determining the jet energy scale. Indeed, such a strategy is already used for anti-k_T jets in the context of pileup mitigation, though further studies are needed to understand systematics in the XCone case.

Ultimately, the choice of jet algorithm should depend on the physics process of interest. For situations with widely separated jets, exclusive cone algorithms like XCone and inclusive cone algorithms like anti-k_T yield rather similar performance, so there is no obvious reason to prefer one algorithm over the other. XCone does have the appealing features of yielding well-defined rigid jet geometries and fitting nicely into N-jettiness factorization theorems (see [1]), though this has to be balanced against the ubiquity, simplicity, and computational efficiency of anti-k_T. For this reason, the advantages of XCone are most prominent in the boosted regime of overlapping (sub)jets, where standard anti-k_T reconstruction is simply not applicable while XCone can dynamically split jet regions.

We have emphasized how XCone allows analysis strategies developed in the more familiar resolved regime to be extrapolated into the boosted regime. One could also adopt the reverse strategy of taking analysis strategies based on boosted jets and extrapolating them into the resolved regime. The HEPTogTagger [50] is an example of this reverse strategy, since it uses fat jets to achieve good signal efficiency at low p_T. The variable R jet algorithm [56] can also be used to implement a reverse strategy, since it can match the jet radius of a fat jet to the p_T of the boosted object of interest. A priori, it is not clear whether resolved-to-boosted or boosted-to-resolved approaches will be more performant, so it is important to develop both types of strategies, as well as hybrid strategies like our $N = 2 \times 3$ method.[10]

---

[10]A similar dichotomy is present for jet grooming methods, where one can take an outside-in approach of first finding a large radius jet and then partitioning it into subjets as in trimming [55], or take an

Given the value of exclusive jet algorithms for lepton colliders but the advantages of conical jets for hadron colliders, we expect that exclusive cone jet algorithms will find useful applications beyond the ones studied in this paper. Because XCone effectively separates jet axis finding from jet region finding, one could even imagine a generalized exclusive cone strategy that dynamically chooses different jet radii R depending on the final state, making it possible to treat even more extreme kinematics. We look forward to seeing how XCone and its generalizations perform in future analyses, as the LHC continues to pursue physics in and beyond the standard model over a wide kinematic range.

Acknowledgments

A Comparison to exclusive k_T

The focus of this paper has been on comparing XCone to anti-k_T, which is essentially comparing an exclusive cone algorithm to an inclusive cone algorithm. It is also instructive to compare XCone to other exclusive non-cone algorithms, which we do in this appendix. Given the popular use of sequential recombination algorithms, the exclusive variants of k_T [8, 58] and Cambridge/Aachen (C/A) [38–40] clustering provide the most useful comparisons.

Because C/A clusters according to angles alone, it turns out to yield rather poor performance when dealing with events with multiple angular scales. This can also be understood from the study in ref. [1], which shows that C/A does not provide good seed axes for N-jettiness minimization. For this reason, we only compare to the exclusive k_T algorithm, as it provides the most similar performance to XCone. Indeed, the $\beta = 1$ minimization procedure in XCone starts from seeds derived from k_T clustering.[11]

As explained in section 2, the distinction between exclusive cone algorithms and inclusive cone algorithms is largely irrelevant in the case of well-separated jets. By contrast, the distinction between cone jets and k_T-style jets is rather important for well-separated jets, especially at large jet radius. Famously, k_T-style jets have distinctly non-conical boundaries which are determined by the configuration of soft radiation within the jet, yielding a broad spectrum of jet areas [16, 17]. For this reason, it is not really fair to compare XCone

---

inside-out approach of first finding small radius jets and then combining them into larger objects as in jets-from-jets [57].

[11]For $\beta = 1$ minimization, XCone uses the winner-take-all recombination scheme [25, 59, 60]. For the exclusive k_T studies here, we stick with standard E-scheme recombination. For $\beta = 2$ minimization, XCone uses a generalized k_T measure halfway between k_T and C/A.

to exclusive k_T with well-separated jets, since XCone simply inherits the advantages of anti-k_T and other cone-like algorithms.

The comparison between XCone and exclusive k_T is most instructive in the boosted regime, where area effects are less important and the distinction between inclusive and exclusive jets is more pronounced. We restrict our attention to $N = 2$ and $N = 3$ boosted Higgs reconstruction (see sections 3.2 and 3.3) and $N = 6$ boosted top reconstruction (see section 4.1). We do not show $N = 2 \times 3$ for boosted tops, since section 4.2 already presented a similar study with exclusive k_T.

A.1 Boosted Higgs bosons with $N = 2$

We saw that XCone with $N = 2$ can reconstruct $H \to b\bar{b}$ decays in both the resolved and boosted regimes, and $N = 3$ can be used to improve performance by accounting for possible ISR in the event. Here, we can repeat the exact same analysis strategy using the exclusive k_T algorithm, with the same choice of $R = 0.5$ and $N = 2, 3$. The XCone distributions shown here are identical to the ones shown in section 3.

The top row of figure 18 shows that the reconstructed Higgs mass distributions are rather similar between the two algorithms, indicating that exclusive k_T also successfully finds the Higgs decay products across a wide kinematic range. However, exclusive k_T has a noticeably larger low-mass tail, indicating that the algorithm does not always capture all of the Higgs decay products. This is due to the irregularity of the resulting k_T jet shapes. As shown in the bottom row of figure 18, the exclusive k_T jet area distributions are rather broad, though they roughly peak at πR^2 as expected. Small-area jets give rise to the low-mass tail while large-area jets are responsible for the high-mass tail. By keeping a more uniform jet area distribution, XCone achieves better Higgs mass resolution.

The Higgs efficiency of the two algorithms is shown in figure 19, using both the $N = 2$ and $N = 3$ methods. Both XCone and exclusive k_T follow a similar pattern, displaying roughly constant efficiencies across the entire p_T range with improved performance going into the boosted regime. XCone yields a higher overall efficiency, though, due to the jet shape issue described above. We conclude that the conical nature of XCone gives it an advantage over exclusive k_T for boosted Higgs reconstruction.

A.2 Boosted top quarks with $N = 6$

The comparison between exclusive k_T and XCone is also instructive for high multiplicity final states, such as boosted top reconstruction. We apply the same analysis strategy as described in section 4.1, comparing exclusive k_T to XCone with $R = 0.5$ and $N = 6$.
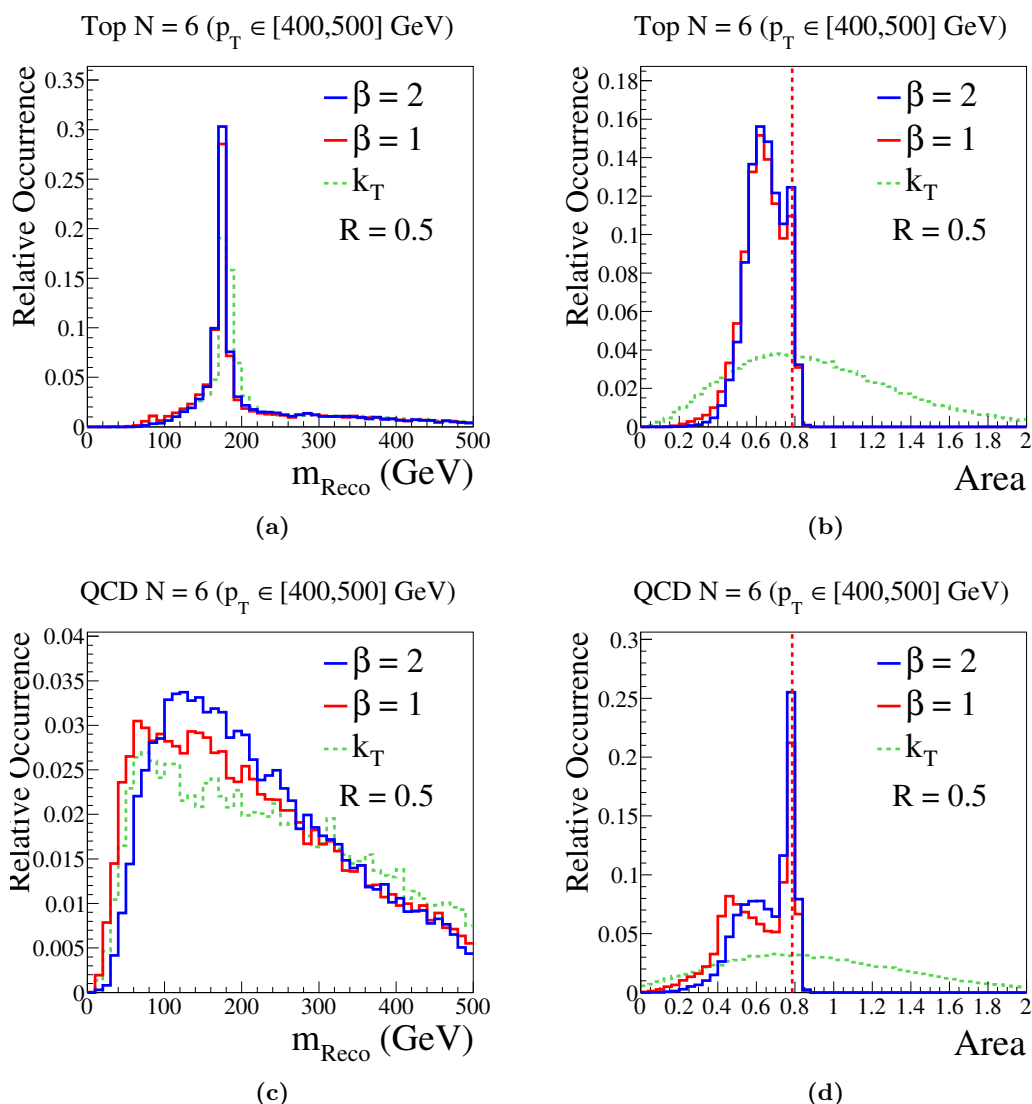
The mass distributions for exclusive k_T jets are shown in the left column of figure 20. For the boosted top signal, the top mass peak is very similar to that of XCone, with a somewhat less pronounced peak and an offset to higher mass values. This same high-mass shift is seen in the QCD background distributions. In the right column of figure 20, one sees again the broad structure of the exclusive k_T jet area distributions. Even though exclusive k_T seems to successfully find the same top decay products as XCone, the jet shapes are rather different, and the high-mass shift is due to the large jet areas sometimes found by exclusive k_T.
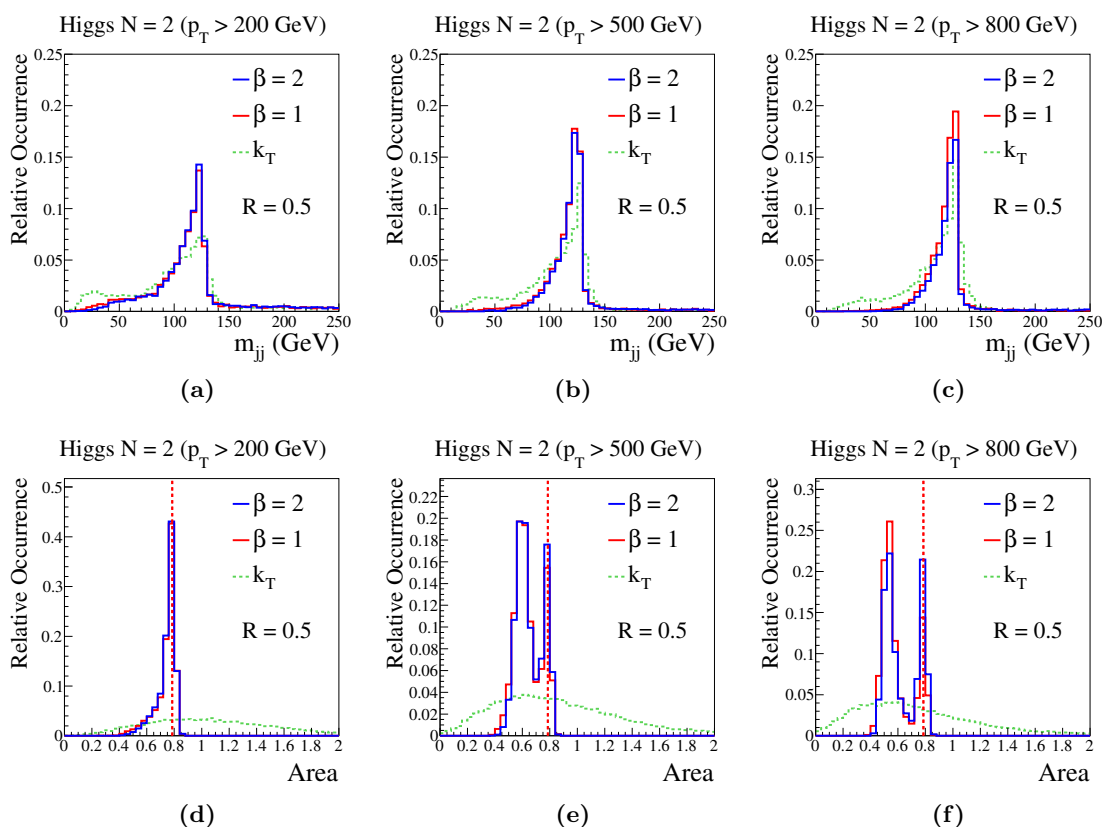
Figure 18. Same as figure 10, but with exclusive k_T. As the Higgs p_T increases from (a) 200 GeV to (b) 500 GeV to (c) 800 GeV, both XCone and exclusive k_T yield a dijet Higgs peak. Exclusive k_T shows a larger low-mass tail, though, indicating that it does not always capture all of the Higgs decay products. This is due to the irregular shape of the k_T jets, as quantified by the jet areas shown in the bottom row.
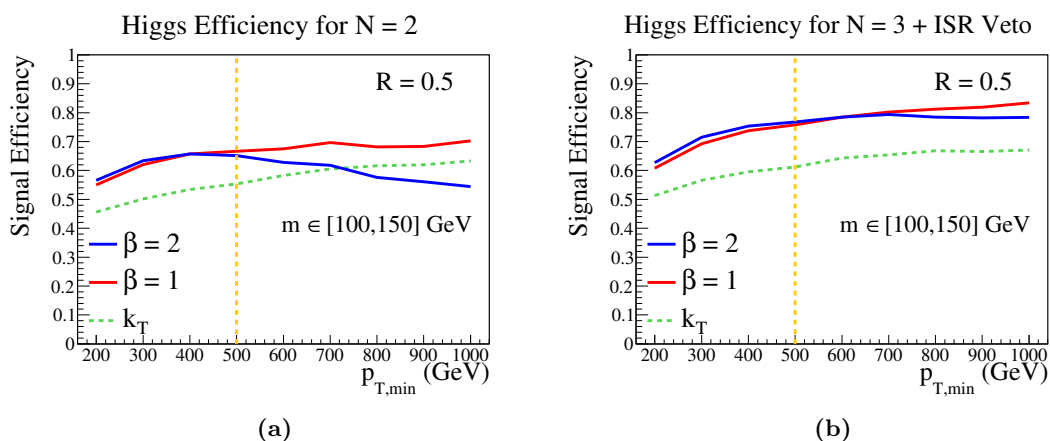
Figure 19. Same as figure 11, but with exclusive k_T. The efficiency of both XCone and exclusive k_T remain roughly constant across the entire kinematic range. XCone shows a distinct advantage over exclusive k_T, however, as its more regular shape allows it to consistently capture the Higgs decay products.
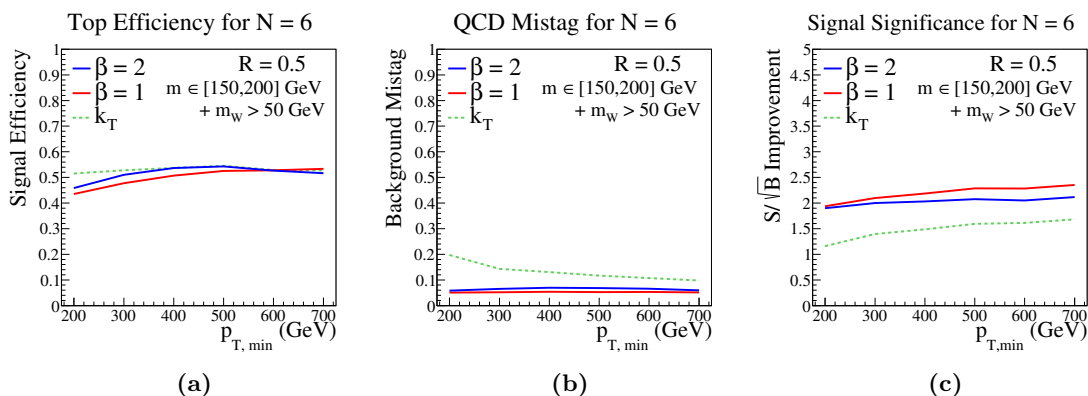
Figure 20. Same as figure 14, but with exclusive k_T. The mass distributions in (a) and (c) are very similar to XCone for both signal and background, but the area distributions in (b) and (d) show that the exclusive k_T jets have a more inconsistent shape than the XCone jets, as expected.

The signal efficiency and background mistag rates are shown in figure 21. The signal efficiency of XCone and exclusive k_T are very similar across the whole p_T range, with exclusive k_T even yielding better performance at low p_T. With exclusive k_T, however, the W mass cut of 50 GeV is less effective at controlling backgrounds, yielding a higher background mistag rate than XCone. This allows XCone to achieve higher signal significance than exclusive k_T.

That said, it may be possible to achieve the same performance gains of XCone by using a hybrid cone and k_T clustering scheme.[12] For example, one could mitigate the high-mass

---
[12]We thank Gavin Salam for discussions on this point.

Figure 21. Same as figure 15, but with exclusive k_T. The signal efficiency is similar between XCone and exclusive k_T, but the background mistag is higher for exclusive k_T, giving XCone the edge in terms of signal significance.

shift coming from large area jets by running an $N = 1$ cone algorithm on each of the $N = 6$ exclusive k_T jets. Alternatively, one could first find the $N = 6$ hardest jets from an inclusive cone algorithm and then run $N = 6$ exclusive k_T on the combined jet constituents. While perhaps not as elegant as XCone, this hybrid approach would still result in a fixed number of approximately conical jets. We leave a study of these hybrid methods for future work.

## B   Background considerations for boosted Higgs

In section 3, we showed that XCone yields excellent signal efficiency for Higgs reconstruction, with an approximately flat response in the case of $N = 2$. While a dedicated background study is beyond the scope of this paper, in this appendix we show that XCone gives sensible results when applied to one of the main background sources: $Z + $ jets. We have not included the effect of b-tagging, though we suspect that XCone would work well with subjet b-tagging methods [46, 47]. We use Pythia 8.176 [27, 28] at the $\sqrt{s} = 14$ TeV LHC to simulate $pp \to Z + $ jets, forcing the Z to decay to neutrinos. As a proxy for the Higgs p_T, we use the recoil p_T of the Z boson. We follow the same analysis strategy as in section 3, showing the background mistag rate for the $N = 1$, $N = 2$, and $N = 3 + $ ISR veto strategies.

As shown in figure 22 for $N = 1$, the reconstructed single jet mass increases for both XCone and anti-k_T as a function of recoil Z p_T. In figure 23, this leads to a mistag rate that increases roughly linearly with p_T, as expected since the invariant mass of an ordinary QCD jet rises as a function of jet p_T. This is part of the reason why jet substructure techniques like mass drop [35] are needed to control the background jet mass distribution. Just as in figure 9, XCone and anti-k_T exhibit very similar performance.

Turning to $N = 2$ in figure 24, the dijet invariant mass spectrum increases with recoil Z p_T, both for XCone and anti-k_T. The reason is that there is no genuine 2-prong structure in the background, so it is far more likely for these algorithms to identify two widely separated jets at large invariant mass rather than two proximate jets at small invariant
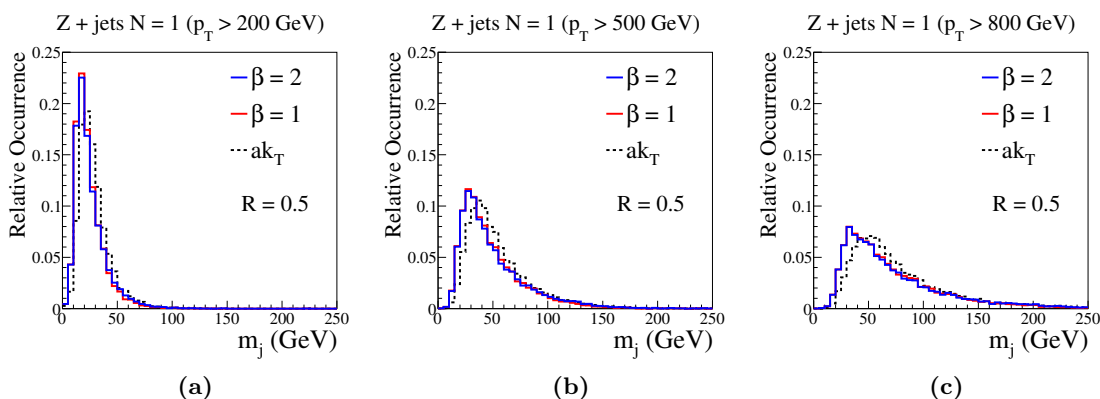
Figure 22. Z + jets reconstruction for $N = 1$, as a potential background to associated Higgs production. As the recoil Z p_T increases from (a) 200 GeV to (b) 500 GeV to (c) 800 GeV, the single jet invariant mass increases, populating the Higgs signal region. See figure 8 for the corresponding signal study.
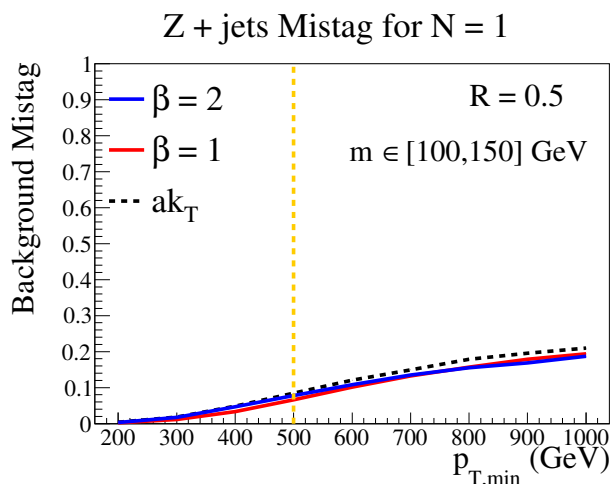
Figure 23. Z+jets mistag rate for $N = 1$ boosted Higgs reconstruction as a function of Z recoil p_T, with the mass window $m_j \in [100, 150]$ GeV. The mistag rate grows with p_T, with similar behavior seen between XCone and anti-k_T. See figure 9 for the corresponding signal study.

mass. In figure 25a, this leads to an approximately flat mistag rate as function of p_T of around 10–15%. As anticipated in the text, the combined $N = 2, 3$ strategy in figure 25b has a higher mistag rate, though it still remains roughly constant as a function of p_T. Though anti-k_T has somewhat better mistag rates than XCone at high p_T, this is also where anti-k_T has low signal efficiencies (recall figure 11).

Note that the above analysis did not include further attempts to mitigate backgrounds through b-tagging, N-subjettiness, or other substructure discriminant variables. Since the mistag rates for XCone and anti-k_T are somewhat similar, we suspect that background mitigation techniques used in current Higgs analyses can be adapted to XCone, though we leave a detailed study to future work.
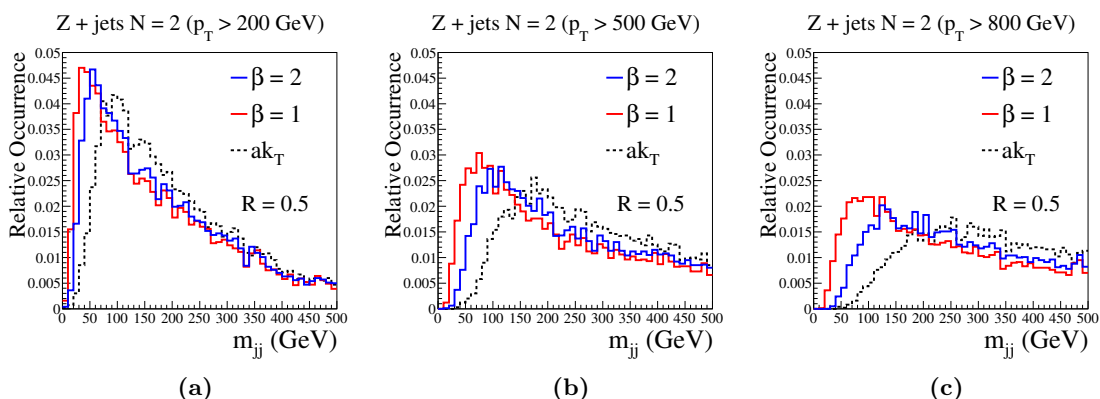
Figure 24. Same as figure 22, but for $N = 2$. As the recoil Z p_T increases from (a) 200 GeV to (b) 500 GeV to (c) 800 GeV, the dijet invariant mass increases, since the two identified jets are unlikely to be proximate in phase space. Note that the scale on the x-axis has been increased compared to figure 22 to include larger jet masses. See figure 10 for the corresponding signal study.
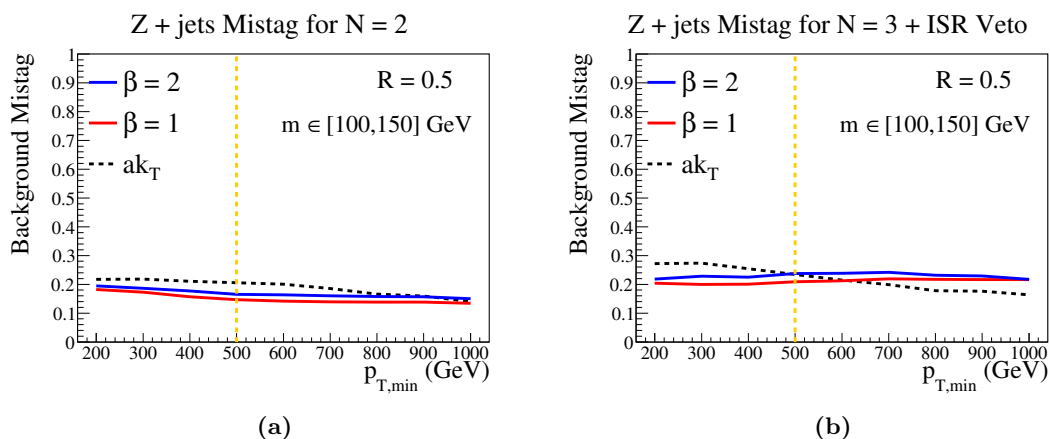

Figure 25. (a) Z+jets mistag rate for $N = 2$ resolved dijet Higgs reconstruction as a function of Z recoil p_T, with the mass window $m_j \in [100, 150]$ GeV. The background rate is nearly constant as a function of p_T, and similar between anti-k_T and XCone, showing that XCone does not unnecessarily sculpt background distributions. (b) Same as figure 11a, but combining $N = 2$ with $N = 3$, using the minimum pairwise mass to veto ISR. Again, we see a roughly flat mistag rate. See figure 11 for the corresponding signal study.

References

[1] I.W. Stewart, F.J. Tackmann, J. Thaler, C.K. Vermilion and T.F. Wilkason, *XCone: N-jettiness as an Exclusive Cone Jet Algorithm*, [*JHEP* **11** (2015) 072](https://doi.org/10.1007/JHEP11(2015)072) [[arXiv:1508.01516](https://arxiv.org/abs/1508.01516)] [[INSPIRE](https://inspirehep.net)].

[2] A. Abdesselam et al., *Boosted objects: A Probe of beyond the Standard Model physics*, [*Eur. Phys. J.* **C 71** (2011) 1661](https://doi.org/10.1140/epjc/s10052-011-1661-y) [[arXiv:1012.5412](https://arxiv.org/abs/1012.5412)] [[INSPIRE](https://inspirehep.net)].

[3] A. Altheimer et al., *Jet Substructure at the Tevatron and LHC: New results, new tools, new benchmarks*, [*J. Phys.* **G 39** (2012) 063001](https://doi.org/10.1088/0954-3899/39/6/063001) [[arXiv:1201.0008](https://arxiv.org/abs/1201.0008)] [[INSPIRE](https://inspirehep.net)].

[4] A. Altheimer et al., *Boosted objects and jet substructure at the LHC. Report of BOOST2012, held at IFIC Valencia, 23rd–27th of July 2012*, [*Eur. Phys. J.* **C 74** (2014) 2792](https://doi.org/10.1140/epjc/s10052-014-2792-8) [[arXiv:1311.2708](https://arxiv.org/abs/1311.2708)] [[INSPIRE](https://inspirehep.net)].

[5] D. Adams et al., *Towards an Understanding of the Correlations in Jet Substructure. Report of BOOST2013, hosted by the University of Arizona, 12th–16th of August 2013*, [*Eur. Phys. J.* **C 75** (2015) 409](https://doi.org/10.1140/epjc/s10052-015-3587-2) [[arXiv:1504.00679](https://arxiv.org/abs/1504.00679)] [[INSPIRE](https://inspirehep.net)].

[6] CMS collaboration, *Searches for new physics using the $t\bar{t}$ invariant mass distribution in pp collisions at $\sqrt{s} = 8\,TeV$*, [*Phys. Rev. Lett.* **111** (2013) 211804](https://doi.org/10.1103/PhysRevLett.111.211804) [[arXiv:1309.2030](https://arxiv.org/abs/1309.2030)] [[INSPIRE](https://inspirehep.net)].

[7] ATLAS collaboration, *Search for resonances decaying into top-quark pairs using fully hadronic decays in pp collisions with ATLAS at $\sqrt{s} = 7\,TeV$*, [*JHEP* **01** (2013) 116](https://doi.org/10.1007/JHEP01(2013)116) [[arXiv:1211.2202](https://arxiv.org/abs/1211.2202)] [[INSPIRE](https://inspirehep.net)].

[8] S. Catani, Y.L. Dokshitzer, M.H. Seymour and B.R. Webber, *Longitudinally invariant K_t clustering algorithms for hadron hadron collisions*, [*Nucl. Phys.* **B 406** (1993) 187](https://doi.org/10.1016/0550-3213(93)90166-M) [[INSPIRE](https://inspirehep.net)].

[9] M. Cacciari, G.P. Salam and G. Soyez, *The anti-k_t jet clustering algorithm*, [*JHEP* **04** (2008) 063](https://doi.org/10.1088/1126-6708/2008/04/063) [[arXiv:0802.1189](https://arxiv.org/abs/0802.1189)] [[INSPIRE](https://inspirehep.net)].

[10] M. Gouzevitch, A. Oliveira, J. Rojo, R. Rosenfeld, G.P. Salam and V. Sanz, *Scale-invariant resonance tagging in multijet events and new physics in Higgs pair production*, [*JHEP* **07** (2013) 148](https://doi.org/10.1007/JHEP07(2013)148) [[arXiv:1303.6636](https://arxiv.org/abs/1303.6636)] [[INSPIRE](https://inspirehep.net)].

[11] G.P. Salam and G. Soyez, *A Practical Seedless Infrared-Safe Cone jet algorithm*, [*JHEP* **05** (2007) 086](https://doi.org/10.1088/1126-6708/2007/05/086) [[arXiv:0704.0292](https://arxiv.org/abs/0704.0292)] [[INSPIRE](https://inspirehep.net)].

[12] M. Stoll, *Vetoed jet clustering: The mass-jump algorithm*, [*JHEP* **04** (2015) 111](https://doi.org/10.1007/JHEP04(2015)111) [[arXiv:1410.4637](https://arxiv.org/abs/1410.4637)] [[INSPIRE](https://inspirehep.net)].

[13] K. Hamaguchi, S.P. Liew and M. Stoll, *How to decontaminate overlapping fat jets*, [*Phys. Rev.* **D 92** (2015) 015012](https://doi.org/10.1103/PhysRevD.92.015012) [[arXiv:1505.02930](https://arxiv.org/abs/1505.02930)] [[INSPIRE](https://inspirehep.net)].

[14] A.J. Larkoski, F. Maltoni and M. Selvaggi, *Tracking down hyper-boosted top quarks*, [*JHEP* **06** (2015) 032](https://doi.org/10.1007/JHEP06(2015)032) [[arXiv:1503.03347](https://arxiv.org/abs/1503.03347)] [[INSPIRE](https://inspirehep.net)].

[15] M. Spannowsky and M. Stoll, *Tracking New Physics at the LHC and beyond*, [*Phys. Rev.* **D 92** (2015) 054033](https://doi.org/10.1103/PhysRevD.92.054033) [[arXiv:1505.01921](https://arxiv.org/abs/1505.01921)] [[INSPIRE](https://inspirehep.net)].

[16] M. Cacciari and G.P. Salam, *Pileup subtraction using jet areas*, [*Phys. Lett.* **B 659** (2008) 119](https://doi.org/10.1016/j.physletb.2007.09.077) [[arXiv:0707.1378](https://arxiv.org/abs/0707.1378)] [[INSPIRE](https://inspirehep.net)].

[17] M. Cacciari, G.P. Salam and G. Soyez, *The Catchment Area of Jets*, *JHEP* **04** (2008) 005 [arXiv:0802.1188] [INSPIRE].

[18] I.W. Stewart, F.J. Tackmann and W.J. Waalewijn, *N-Jettiness: An Inclusive Event Shape to Veto Jets*, *Phys. Rev. Lett.* **105** (2010) 092002 [arXiv:1004.2489] [INSPIRE].

[19] J. Thaler and K. Van Tilburg, *Identifying Boosted Objects with N-subjettiness*, *JHEP* **03** (2011) 015 [arXiv:1011.2268] [INSPIRE].

[20] J. Thaler and K. Van Tilburg, *Maximizing Boosted Top Identification by Minimizing N-subjettiness*, *JHEP* **02** (2012) 093 [arXiv:1108.2701] [INSPIRE].

[21] T.T. Jouttenus, I.W. Stewart, F.J. Tackmann and W.J. Waalewijn, *Jet mass spectra in Higgs boson plus one jet at next-to-next-to-leading logarithmic order*, *Phys. Rev.* **D 88** (2013) 054031 [arXiv:1302.0846] [INSPIRE].

[22] J.-H. Kim, *Rest Frame Subjet Algorithm With SISCone Jet For Fully Hadronic Decaying Higgs Search*, *Phys. Rev.* **D 83** (2011) 011502 [arXiv:1011.1493] [INSPIRE].

[23] J. Thaler, *Jet maximization, axis minimization and stable cone finding*, *Phys. Rev.* **D 92** (2015) 074001 [arXiv:1506.07876] [INSPIRE].

[24] S.D. Ellis, J. Huston and M. Tonnesmann, *On building better cone jet algorithms*, *eConf* **C 010630** (2001) 513 [hep-ph/0111434] [INSPIRE].

[25] A.J. Larkoski, D. Neill and J. Thaler, *Jet Shapes with the Broadening Axis*, *JHEP* **04** (2014) 017 [arXiv:1401.2158] [INSPIRE].

[26] A.J. Larkoski and J. Thaler, *Aspects of jets at* 100 *TeV*, *Phys. Rev.* **D 90** (2014) 034010 [arXiv:1406.7011] [INSPIRE].

[27] T. Sjöstrand, S. Mrenna and P.Z. Skands, *PYTHIA 6.4 Physics and Manual*, *JHEP* **05** (2006) 026 [hep-ph/0603175] [INSPIRE].

[28] T. Sjöstrand, S. Mrenna and P.Z. Skands, *A Brief Introduction to PYTHIA 8.1*, *Comput. Phys. Commun.* **178** (2008) 852 [arXiv:0710.3820] [INSPIRE].

[29] M. Cacciari, G.P. Salam and G. Soyez, *FastJet User Manual*, *Eur. Phys. J.* **C 72** (2012) 1896 [arXiv:1111.6097] [INSPIRE].

[30] *Fastjet contrib*, http://fastjet.hepforge.org/contrib/.

[31] M. Dasgupta, L. Magnea and G.P. Salam, *Non-perturbative QCD effects in jets at hadron colliders*, *JHEP* **02** (2008) 055 [arXiv:0712.3014] [INSPIRE].

[32] CMS collaboration, *Search for the standard model Higgs boson produced in association with a W or a Z boson and decaying to bottom quarks*, *Phys. Rev.* **D 89** (2014) 012003 [arXiv:1310.3687] [INSPIRE].

[33] ATLAS collaboration, *Search for the $b\bar{b}$ decay of the Standard Model Higgs boson in associated $(W/Z)H$ production with the ATLAS detector*, *JHEP* **01** (2015) 069 [arXiv:1409.6212] [INSPIRE].

[34] J. Gallicchio, J. Huth, M. Kagan, M.D. Schwartz, K. Black and B. Tweedie, *Multivariate discrimination and the Higgs +W/Z search*, *JHEP* **04** (2011) 069 [arXiv:1010.3698] [INSPIRE].

[35] J.M. Butterworth, A.R. Davison, M. Rubin and G.P. Salam, *Jet substructure as a new Higgs search channel at the LHC*, *Phys. Rev. Lett.* **100** (2008) 242001 [arXiv:0802.2470] [INSPIRE].

[36] J.M. Butterworth, I. Ochoa and T. Scanlon, *Boosted Higgs $\rightarrow b\bar{b}$ in vector-boson associated production at 14 TeV*, *Eur. Phys. J.* **C 75** (2015) 366 [arXiv:1506.04973] [inSPIRE].

[37] G.D. Kribs, A. Martin, T.S. Roy and M. Spannowsky, *Discovering the Higgs Boson in New Physics Events using Jet Substructure*, *Phys. Rev.* **D 81** (2010) 111501 [arXiv:0912.4731] [inSPIRE].

[38] Y.L. Dokshitzer, G.D. Leder, S. Moretti and B.R. Webber, *Better jet clustering algorithms*, *JHEP* **08** (1997) 001 [hep-ph/9707323] [inSPIRE].

[39] M. Wobisch and T. Wengler, *Hadronization corrections to jet cross-sections in deep inelastic scattering*, hep-ph/9907280 [inSPIRE].

[40] M. Wobisch, *Measurement and QCD analysis of jet cross-sections in deep inelastic positron proton collisions at $\sqrt{s} = 300\,GeV$*, DESY-THESIS-2000-049 (2000) [inSPIRE].

[41] G.C. Blazey et al., *Run II jet physics*, hep-ex/0005012 [inSPIRE].

[42] G. Brooijmans, *High pT Hadronic Top Quark Identification. Part 1: Jet Mass and YSplitter*, ATL-PHYS-CONF-2008-008 (2008) [inSPIRE].

[43] J. Thaler and L.-T. Wang, *Strategies to Identify Boosted Tops*, *JHEP* **07** (2008) 092 [arXiv:0806.0023] [inSPIRE].

[44] D.E. Kaplan, K. Rehermann, M.D. Schwartz and B. Tweedie, *Top Tagging: A Method for Identifying Boosted Hadronically Decaying Top Quarks*, *Phys. Rev. Lett.* **101** (2008) 142001 [arXiv:0806.0848] [inSPIRE].

[45] L.G. Almeida, S.J. Lee, G. Perez, G.F. Sterman, I. Sung and J. Virzi, *Substructure of high-p_T Jets at the LHC*, *Phys. Rev.* **D 79** (2009) 074017 [arXiv:0807.0234] [inSPIRE].

[46] CMS collaboration, *Performance of b tagging at $\sqrt{s} = 8\,TeV$ in multijet, $t\bar{t}$ and boosted topology events*, CMS-PAS-BTV-13-001 (2013) [inSPIRE].

[47] ATLAS collaboration, *Flavor Tagging with Track Jets in Boosted Topologies with the ATLAS Detector*, ATL-PHYS-PUB-2014-013 (2014).

[48] D. Curtin, R. Essig and B. Shuve, *Boosted Multijet Resonances and New Color-Flow Variables*, *Phys. Rev.* **D 88** (2013) 034019 [arXiv:1210.5523] [inSPIRE].

[49] CMS collaboration, *Boosted Top Jet Tagging at CMS*, CMS-PAS-JME-13-007 (2014) [inSPIRE].

[50] T. Plehn, M. Spannowsky, M. Takeuchi and D. Zerwas, *Stop Reconstruction with Tagged Tops*, *JHEP* **10** (2010) 078 [arXiv:1006.2833] [inSPIRE].

[51] T. Plehn, G.P. Salam and M. Spannowsky, *Fat Jets for a Light Higgs*, *Phys. Rev. Lett.* **104** (2010) 111801 [arXiv:0910.5472] [inSPIRE].

[52] S. Fleming, A.H. Hoang, S. Mantry and I.W. Stewart, *Top Jets in the Peak Region: Factorization Analysis with NLL Resummation*, *Phys. Rev.* **D 77** (2008) 114003 [arXiv:0711.2079] [inSPIRE].

[53] S. Fleming, A.H. Hoang, S. Mantry and I.W. Stewart, *Jets from massive unstable particles: Top-mass determination*, *Phys. Rev.* **D 77** (2008) 074010 [hep-ph/0703207] [inSPIRE].

[54] M. Freytsis, T. Volansky and J.R. Walsh, *Tagging Partially Reconstructed Objects with Jet Substructure*, arXiv:1412.7540 [inSPIRE].

[55] D. Krohn, J. Thaler and L.-T. Wang, *Jet Trimming*, *JHEP* **02** (2010) 084 [arXiv:0912.1342] [InSPIRE].

[56] D. Krohn, J. Thaler and L.-T. Wang, *Jets with Variable R*, *JHEP* **06** (2009) 059 [arXiv:0903.0392] [InSPIRE].

[57] B. Nachman, P. Nef, A. Schwartzman, M. Swiatlowski and C. Wanotayaroj, *Jets from Jets: Re-clustering as a tool for large radius jet reconstruction and grooming at the LHC*, *JHEP* **02** (2015) 075 [arXiv:1407.2922] [InSPIRE].

[58] S.D. Ellis and D.E. Soper, *Successive combination jet algorithm for hadron collisions*, *Phys. Rev.* **D 48** (1993) 3160 [hep-ph/9305266] [InSPIRE].

[59] D. Bertolini, T. Chan and J. Thaler, *Jet Observables Without Jet Algorithms*, *JHEP* **04** (2014) 013 [arXiv:1310.7584] [InSPIRE].

[60] G. Salam, E_t^∞ *Scheme*, unpublished.